

AeroDyn Theory Manual

Patrick J. Moriarty

National Renewable Energy Laboratory

Golden, Colorado

A. Craig Hansen

Windward Engineering

Salt Lake City, Utah



NREL

National Renewable Energy Laboratory

1617 Cole Boulevard, Golden, Colorado 80401-3393

303-275-3000 • www.nrel.gov

Operated for the U.S. Department of Energy
Office of Energy Efficiency and Renewable Energy
by Midwest Research Institute • Battelle

AeroDyn Theory Manual

Patrick J. Moriarty

National Renewable Energy Laboratory

Golden, Colorado

A. Craig Hansen

Windward Engineering

Salt Lake City, Utah

Prepared under Task No. WER43101, WER53101



NREL

National Renewable Energy Laboratory

1617 Cole Boulevard, Golden, Colorado 80401-3393

303-275-3000 • www.nrel.gov

Operated for the U.S. Department of Energy
Office of Energy Efficiency and Renewable Energy
by Midwest Research Institute • Battelle

NOTICE

This report was prepared as an account of work sponsored by an agency of the United States government. Neither the United States government nor any agency thereof, nor any of their employees, makes any warranty, express or implied, or assumes any legal liability or responsibility for the accuracy, completeness, or usefulness of any information, apparatus, product, or process disclosed, or represents that its use would not infringe privately owned rights. Reference herein to any specific commercial product, process, or service by trade name, trademark, manufacturer, or otherwise does not necessarily constitute or imply its endorsement, recommendation, or favoring by the United States government or any agency thereof. The views and opinions of authors expressed herein do not necessarily state or reflect those of the United States government or any agency thereof.

Available electronically at <http://www.osti.gov/bridge>

Available for a processing fee to U.S. Department of Energy and its contractors, in paper, from:

U.S. Department of Energy
Office of Scientific and Technical Information
P.O. Box 62
Oak Ridge, TN 37831-0062
phone: 865.576.8401
fax: 865.576.5728
email: <mailto:reports@adonis.osti.gov>

Available for sale to the public, in paper, from:

U.S. Department of Commerce
National Technical Information Service
5285 Port Royal Road
Springfield, VA 22161
phone: 800.553.6847
fax: 703.605.6900
email: orders@ntis.fedworld.gov
online ordering: <http://www.ntis.gov/ordering.htm>



Abstract

AeroDyn is a set of routines used in conjunction with an aeroelastic simulation code to predict the aerodynamics of horizontal axis wind turbines. These subroutines provide several different models whose theoretical bases are described in this manual. AeroDyn contains two models for calculating the effect of wind turbine wakes: the blade element momentum theory and the generalized dynamic-wake theory. Blade element momentum theory is the classical standard used by many wind turbine designers and generalized dynamic wake theory is a more recent model useful for modeling skewed and unsteady wake dynamics. When using the blade element momentum theory, various corrections are available for the user, such as incorporating the aerodynamic effects of tip losses, hub losses, and skewed wakes. With the generalized dynamic wake, all of these effects are automatically included. Both of these methods are used to calculate the axial induced velocities from the wake in the rotor plane. The user also has the option of calculating the rotational induced velocity. In addition, AeroDyn contains an important model for dynamic stall based on the semi-empirical Beddoes-Leishman model. This model is particularly important for yawed wind turbines. Another aerodynamic model in AeroDyn is a tower shadow model based on potential flow around a cylinder and an expanding wake. Finally, AeroDyn has the ability to read several different formats of wind input, including single-point hub-height wind files or multiple-point turbulent winds.

Table of Contents

| | |
|---|-----|
| Abstract | iii |
| Nomenclature | vi |
| Introduction | 1 |
| Wake Modeling | 2 |
| Blade Element Momentum | 2 |
| Tip-Loss Model..... | 5 |
| Hub-Loss Model | 6 |
| Glauert Correction | 6 |
| Skewed Wake Correction | 7 |
| Other Corrections..... | 9 |
| Final Iteration Procedure for Blade Element Momentum Theory | 9 |
| Generalized Dynamic Wake | 11 |
| Basic Derivation..... | 12 |
| Pressure Distribution..... | 13 |
| Induced Velocity Distribution..... | 15 |
| Expansion of Governing Equation..... | 16 |
| Flow Parameters..... | 18 |
| Pressure Coefficients | 18 |
| Final Governing Equations | 19 |
| Procedure for Generalized Dynamic Wake Calculations | 19 |
| Airfoil Aerodynamics..... | 21 |
| Static Airfoil Characteristics..... | 22 |
| Dynamic Stall Model | 23 |
| Model Modifications..... | 26 |
| Tower Influence..... | 30 |
| Wind Input Files | 32 |
| Possible Improvements | 33 |
| References..... | 34 |

List of Figures

| | |
|--|----|
| Figure 1. Annular plane used in blade element momentum theory | 2 |
| Figure 2. Local element velocities and flow angles..... | 3 |
| Figure 3. Local elemental forces..... | 3 |
| Figure 4. Helical wake pattern of single tip vortex..... | 4 |
| Figure 5. Tip-loss factor for blade with constant 10° inflow angle along span (optimal twist) | 5 |
| Figure 6. Glauert correction for tip-loss factor, $F = 1.0$ | 7 |
| Figure 7. Glauert correction for tip-loss factor, $F = 0.75$ | 7 |
| Figure 8. Coordinates used in skewed wake correction..... | 8 |
| Figure 9. Generator power output during rapid pitch changes (from 0.2° to 3.9° and back) for the Tjæreborg turbine, Suzuki (2000)..... | 12 |
| Figure 10. Contours of constant v in the x-z plane..... | 14 |
| Figure 11. Contours of constant η in the x-z plane..... | 14 |
| Figure 12. Velocities and coordinates used in the GDW model..... | 18 |
| Figure 13. Lift coefficient for S809 airfoil at Reynolds number of 750 million. | 22 |
| Figure 14. Drag coefficient for S809 airfoil at Reynolds number of 750 million. | 22 |
| Figure 15. Dynamic stall events measured at the 30% station of the CER (Pierce 1996)..... | 24 |
| Figure 16. Coordinate system and forces used in dynamic stall modeling..... | 24 |
| Figure 17. Typical attached flow unsteady response of the normal force coefficient | 24 |
| Figure 18. Typical normal coefficient response of an airfoil with attached flow modified by separation point..... | 25 |
| Figure 19. Unsteady separation point curve | 25 |
| Figure 20. Typical normal coefficient response of an airfoil with attached flow, separation point, and vortex lift contribution | 26 |
| Figure 21. Exponential curve fit to the calculated separation point for a NACA 4415..... | 27 |
| Figure 22. Comparison between data and reproduced curve using exponential curve fit to separation point data (NACA 4415) | 27 |
| Figure 23. Normal and chordwise coefficient separation point curves for a NACA 4415..... | 27 |
| Figure 24. Comparison between measured and reproduced lift coefficient (NACA 4415) | 28 |
| Figure 25. Comparison between measured C_D , C_D reproduced using the current method, and C_D reproduced by method of Beddoes using curve fit C_N separation point (NACA 4415) | 28 |
| Figure 26. Dynamic normal force coefficient simulations for unusual angles of attack (NACA 4415)..... | 29 |
| Figure 27. Schematic of the tower shadow model with parameters illustrated for a given point.. | 32 |
| Figure 28. Coordinate system used for wind input files | 33 |

Nomenclature

Blade Element Momentum Model

| | |
|-------------|---|
| a | = axial induction factor |
| a_{skew} | = axial induction factor with skewed wake |
| a' | = rotational or tangential induction factor |
| B | = number of blades |
| c | = chord length |
| C_l | = lift coefficient |
| C_d | = drag coefficient |
| C_T | = thrust coefficient |
| dr | = blade element and annulus width |
| dQ | = torque of element or annulus |
| dT | = thrust of element or annulus |
| D | = drag force |
| F | = combined tip-loss and hub-loss coefficient |
| L | = lift force |
| r | = local radius |
| Q | = torque |
| R | = rotor radius |
| R_{hub} | = hub radius |
| T | = thrust |
| U_∞ | = mean wind speed |
| v_{e-ip} | = in-plane element velocity due to blade motion |
| v_{e-op} | = out-of-plane element velocity due to blade motion |
| V_{Total} | = total velocity seen by blade element |
| α | = local angle of attack |
| β | = local element pitch angle |
| γ | = yaw inflow angle |
| φ | = local flow angle |
| λ_r | = local tip speed ratio = $\frac{\Omega r}{U_\infty}$ |
| σ' | = local solidity = $\frac{Bc}{2\pi r}$ |
| ρ | = air density |
| χ | = rotor wake angle |
| ψ | = azimuth angle |
| Ω | = rotor rotational speed |

Generalized Dynamic Wake Model

| | |
|---------|---|
| A | = rotor area = πR^2 |
| A_e | = effective rotor area = $\pi(R^2 - R_H^2)$ |
| B | = number of rotor blades |
| C_n^m | = arbitrary constant for generalized dynamic wake model |
| D_n^m | = arbitrary constant for generalized dynamic wake model |

- i = imaginary number = $\sqrt{-1}$
 i = integer index
 j, n = polynomial number (integers)
 L_i^q = aerodynamic force normal to the rotor plane acting on blade element i of blade q
 $[L]$ = inflow gain matrix
 $[\tilde{L}]$ = portion of inflow gain matrix dependent on the wake skew angle
 m, r = harmonics number (integers)
 $[M]$ = apparent mass matrix
 N_E = number of blade elements in a blade
 p = pressure
 P_n^m = associated Legendre function of the first kind
 \hat{P}_n^m = normalized associated Legendre function of the first kind
 $\hat{P}_n^m(v) = (-1)^m P_n^m(v) / \rho_n^m$
 Q_n^m = associated Legendre function of the second kind
 \hat{Q}_n^m = normalized associated Legendre function of the second kind
 $\hat{Q}_n^m(i\eta) = Q_n^m(i\eta) / Q_n^m(i0)$
 R = rotor outer radius
 r = harmonics number (integers), if used in conjunction with a summation symbol (Σ)
 r = radius
 r_i = radius of the i^{th} element
 \hat{r} = dimensionless radius
 R_i = outer radius of annular section i
 R_H = rotor hinge radius
 t = time
 \hat{t} = dimensionless time = Ωt (= ψ , if $\psi_0 = \psi|_{t=0} = 0$)
 u_i = induced velocity in i^{th} direction
 \hat{u}_i = dimensionless induced velocity in i^{th} direction
 V = incoming flow velocity nondimensionalized by ΩR , = $\frac{\mu^2 + (\lambda + \lambda_m)\lambda}{\sqrt{\mu^2 + \lambda^2}}$
 $[\hat{V}]$ = flow parameter matrix
 V_T = total flow velocity at rotor plane nondimensionalized by ΩR , = $\sqrt{\mu^2 + \lambda^2}$
 U_∞ = free stream wind speed = $|\vec{U}_\infty|$
 x_i = displacement in i^{th} direction
 X = function of wake skew angle, χ . $X = \tan|\chi/2|$
 α_d = inflow angle, the angle between the inflow and the rotor plane
 α = wake skew angle, the angle between the mean wake path and the rotor plane
 α_j^r = induced-velocity expansion coefficient for the cosine part
 β_j^r = induced-velocity expansion coefficient for the sine part
 χ = total wake skew angle. The angle between the mean wake path and the rotor axis. The

wake is normal to the rotor if $\chi = 0$, and in-plane if $\chi = \pi/2$.

$$\chi = \pi/2 - \alpha \text{ and } 0 \leq \chi \leq \pi/2.$$

Φ = nondimensional pressure = $\Phi^A + \Phi^V$

Φ^A = nondimensional pressure due to unsteadiness

Φ^V = nondimensional pressure due to convection

$\phi_j^r(\bar{r})$ = radial expansion shape function, $\phi_j^r(\bar{r}) = \frac{1}{\nu} \bar{P}_j^r(\nu)$; $\nu = \sqrt{1 - \bar{r}^2}$

λ = total inflow velocity, nondimensionalized by blade tip speed (ΩR), $\lambda = \lambda_f + \lambda_m$

λ_f = total inflow due to free-stream wind, nondimensionalized by blade tip speed

$$= V \sin \alpha_d$$

λ_m = momentum-theory induced velocity nondimensionalized by blade tip speed

μ = advance ratio, in-plane incoming velocity nondimensionalized by blade tip speed

$$= V \cos \alpha_d$$

ν, η, ψ = ellipsoidal coordinates defined as follows:

$$x = \sqrt{1 - \nu^2} \sqrt{1 + \eta^2} \cos \psi$$

$$y = \sqrt{1 - \nu^2} \sqrt{1 + \eta^2} \sin \psi$$

$$z = \nu \eta$$

ρ = air density

ρ_n^m = integral of the associated Legendre function of the first kind from 0 to 1,

$$\rho_n^m = \int_0^1 [P_n^m(\nu)]^2 d\nu$$

τ_n^{mC} = cosine part of pressure coefficient

τ_n^{mS} = sine part of pressure coefficient

Superscripts

$()^*$ = first derivative with respect to the nondimensional time, \hat{t} . $()^* = d/d\hat{t}$

$(\hat{\quad})$ = nondimensional quantity

$()^C$ = index for cosine terms

$()^S$ = index for sine terms

Dynamic Stall Model

C_C = chordwise force coefficient

C_D = drag coefficient

C_{D0} = minimum drag coefficient

C_L = lift coefficient

C_N = normal-force coefficient

C'_N = normal-force coefficient with first order lag and attached flow

C_{NI} = normal-force coefficient at stall

ΔC_N^C = increment in normal-force coefficient, circulatory component

ΔC_N^I = increment in normal-force coefficient, non-circulatory component

$C_{N\alpha}$ = normal-force coefficient curve slope
 f = separation-point distance from leading edge normalized by chord length
 M = Mach number
 α = angle of attack
 α_0 = zero-lift angle of attack
 $\Delta\alpha$ = step change in angle of attack
 τ_v = vortex-travel dimensionless time constant
 ϕ_α^C = circulatory indicial function
 ϕ_α^I = non-circulatory indicial function

Tower Wake Model

C_d = tower-drag coefficient (based on diameter)
 d = dimensionless radial distance from tower center
 u = dimensionless horizontal wind component (x-direction)
 u_{wake} = dimensionless wake-velocity deficit
 v = dimensionless horizontal wind component (y-direction)
 x = dimensionless wind-field coordinate, downwind
 y = dimensionless wind-field coordinate, left when looking downwind
 U_{local} = total velocity in x-direction
 V_{local} = total velocity in y-direction
 U_∞ = total wind speed (mean and any turbulent fluctuation)

Wind Input

x, y, z = coordinates measured from the hub location (x is usually south and z is vertical up)
 $Hshr$ = linear-shear coefficients in the horizontal direction
 V_{gust} = gust velocity
 V_{hub} = hub wind speed
 $Vshr$ = vertical-shear power-law exponent
 $Vshr_{lin}$ = linear-shear coefficients in the vertical direction
 δ = wind direction angle from x-axis
 γ = rotor-plane yaw angle relative to x-axis

Introduction

AeroDyn is a series of routines written to perform the aerodynamic calculations for aeroelastic simulations of horizontal axis wind turbine configurations. Craig Hansen and researchers at the University of Utah and Windward Engineering originally developed these routines for wind turbine simulation work, and the complexity of the algorithms has gradually increased with time. Recently, researchers at the National Renewable Energy Laboratory (NREL) have further developed these routines and changes are ongoing. This report provides users of these routines with the aerodynamic theories behind the various algorithms in AeroDyn. It also provides some insight into the limits of each aerodynamic model, which may provide ideas for further improvement. This report is not intended to be a user's guide for the routines, however. That kind of guide (Laino and Hansen 2002) is available for downloading at the NREL design codes Web site (<http://wind.nrel.gov/designcodes/>).

Currently, the routines of AeroDyn interface with several aeroelastic simulation codes: YawDyn, FAST, SymDyn, and ADAMS. The differences between these codes lie mainly in the structural dynamics, and since each of them uses AeroDyn, the aerodynamic calculations between them are identical. Further explanation and user's guides for each of these codes are also on the NREL design codes Web site.

When called from the aeroelastic simulation routines, AeroDyn calculates the aerodynamic lift, drag, and pitching moment of airfoil sections along the wind turbine blades. It does this by first breaking each blade into a number of segments along the span, as specified by an AeroDyn input file. AeroDyn concurrently gathers information about the turbine geometry, operating condition, blade-element velocity and location, and wind inflow from input files and the aeroelastic simulation program. It then uses this information to calculate the various forces for each segment, which are used by the aeroelastic simulation program to calculate the distributed forces on the turbine blades. The aerodynamic forces affect the turbine deflections and vice versa, making the interaction fully aeroelastic. AeroDyn models use relations based on two-dimensional localized flow, and the characteristics of the airfoils along the blade are represented typically by lift, drag, and pitching moment coefficients measured in wind tunnel tests. The wind input can consist of a wide variety of atmospheric conditions: three-dimensional and time-varying atmospheric turbulence as well as discrete gusts or steady mean wind speeds. Often, these wind inputs are produced by another NREL simulation code, TurbSim (Jonkman and Buhl 2004). These winds and the AeroDyn calculations are all limited to time domain calculations. Typically, AeroDyn is called by the aeroelastic simulator at each time step to calculate the changing aerodynamic forces.

Several different aerodynamic models are used in AeroDyn and the user of the routines has the option of selecting which of these are most applicable to their simulation needs. The most important of these aerodynamic models are the wake models. AeroDyn contains two wake models: the blade element momentum theory and the generalized dynamic wake theory, both of which are explained in detail below. The user also has the option of turning off the wake completely, which is useful for modeling parked turbines or debugging input files. If the user chooses blade element momentum theory, there are also options to incorporate the aerodynamic effects of tip losses, hub losses, and skewed wake. With the generalized dynamic wake, all of these effects are automatically included. Both of these methods are used to calculate the axial induced velocities from the wake in the rotor plane. The user also has the option of calculating the rotational (or tangential) induced velocity, which affects the rotor torque. AeroDyn also contains another important model for dynamic stall based on the semi-empirical Beddoes-

Leishman model. This model is particularly important for skewed wind turbines and is explained in more detail below. The final aerodynamic model in AeroDyn is a tower shadow model based on potential flow around a circular cylinder, and it is also explained below.

Wake Modeling

The user has two different options for calculating the effect of the wake on the turbine rotor aerodynamics: either the classic blade element momentum theory or the more recently developed generalized dynamic wake model. Each model is explained in more detail in the following sections.

Blade Element Momentum

Blade element momentum (BEM) theory is one of the oldest and most commonly used methods for calculating induced velocities on wind turbine blades. This theory is an extension of actuator disk theory, first proposed by the pioneering propeller work of Rankine and Froude in the late 19th century. The BEM theory, generally attributed to Betz and Glauert (1935), actually originates from two different theories: blade element theory and momentum theory (see Leishman 2000). Blade element theory assumes that blades can be divided into small elements that act independently of surrounding elements and operate aerodynamically as two-dimensional airfoils whose aerodynamic forces can be calculated based on the local flow conditions. These elemental forces are summed along the span of the blade to calculate the total forces and moments exerted on the turbine. The other half of BEM, the momentum theory, assumes that the loss of pressure or momentum in the rotor plane is caused by the work done by the airflow passing through the rotor plane on the blade elements. Using the momentum theory, one can calculate the induced velocities from the momentum lost in the flow in the axial and tangential directions. These induced velocities affect the inflow in the rotor plane and therefore also affect the forces calculated by blade element theory. This coupling of two theories ties together blade element momentum theory and sets up an iterative process to determine the aerodynamic forces and also the induced velocities near the rotor.

In practice, BEM theory is implemented by breaking the blades of a wind turbine into many elements along the span. As these elements rotate in the rotor plane, they trace out annular regions, shown in Figure 1, across which the momentum balance takes place. These annular regions are also where the induced velocities from the wake change the local flow velocity at the rotor plane. BEM can also be used to analyze stream tubes through the rotor disk, which can be smaller than the annular regions and provide more computational fidelity. However, as currently written, AeroDyn only allows analysis using annular regions.

Because of its simplicity, BEM theory does have its limitations. One primary assumption is that the calculations are static; it is assumed that the airflow field around the airfoil is always in equilibrium and that the passing flow accelerates instantaneously to adjust to the changes in the vorticity in the wake. In practice, it has been shown that the airfoil response takes time to adjust to a changing wake resulting from new inflow or turbine operating conditions (Snel and Schepers 1995). In order to model this time lag effect correctly, we recommended that the user utilize the generalized dynamic wake model described below. One other limitation is that BEM theory

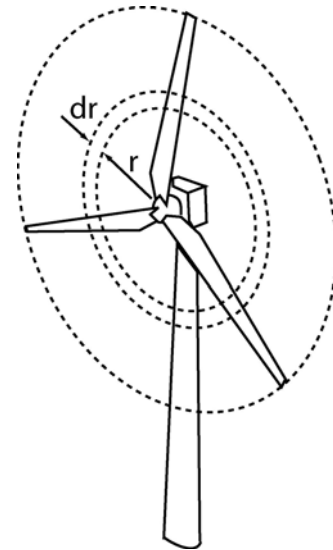


Figure 1. Annular plane used in blade element momentum theory

breaks down when the blades experience large deflections out of the rotor plane. Because the theory assumes that momentum is balanced in a plane parallel to the rotor, any deflections of the rotor will lead to errors in the aerodynamic modeling. Another limitation of BEM theory comes from blade element theory. This theory is based on the assumption that the forces acting on the blade element are essentially two-dimensional, meaning that spanwise flow is neglected. This assumption also implies that there is very little spanwise pressure variation (which would create spanwise flow), and the theory is therefore less accurate for heavily loaded rotors with large pressure gradients across the span. Some other limitations of the original theory include no modeling of tip or hub vortex influence on the induced velocities and an inability to account for skewed inflow. However, corrections to the original theory have provided some methods to model these aerodynamic effects and will be explained in more detail below. In spite of the limitations listed above, BEM theory has been used widely as a reliable model for calculating the induced velocity and elemental forces on wind turbine blades, and it has been retained as a useful model in AeroDyn.

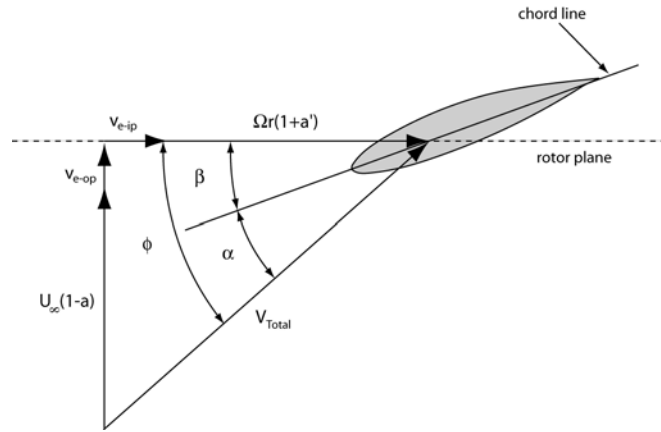


Figure 2. Local element velocities and flow angles

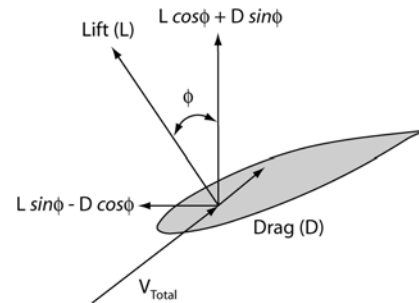


Figure 3. Local elemental forces

The advantage of the BEM theory is that each blade element is modeled as a two-dimensional airfoil. Figure 2 is an example of an airfoil with the velocities and angles that determine the forces on the element and also the induced velocities from the wake influence. Figure 3 shows the resultant aerodynamic forces on the element and their components perpendicular and parallel to the rotor plane. These are the forces that dictate the thrust (perpendicular) and torque (parallel) of the rotor, which are the dominant forces for turbine design. In Figure 3, the angle relating the lift and drag of the airfoil element to the thrust and torque forces is the local inflow angle, ϕ (or ϕ in the figures). As shown in Figure 2, this inflow angle is the sum of the local pitch angle of the blade, β , and the angle of attack, α . The local pitch angle is dependent on the static blade geometry, elastic deflections, and the active or passive blade pitch control system. The angle of attack is a function of the local velocity vector, which is in turn constrained by the incoming local wind speed, rotor speed, blade element velocities and induced velocities. Note in Figure 2 that the velocities of the element from blade deflections (v_{e-op} and v_{e-ip}) affect the inflow angle and angle of attack, but are not directly affected by the induced velocities from the wake. This assumption is consistent with momentum theory, but it might not be the appropriate physical model for the element-wake coupling.

Because we are required to obtain the angle of attack to determine the aerodynamic forces on an element, we must first determine the inflow angle based on the two components of the local velocity vector. Assuming that the blade motion is very small, the resulting equation is dependent on the induced velocities in both the axial and tangential directions as well as the local tip speed ratio:

$$\tan \varphi = \frac{U_\infty(1-a)}{\Omega r(1+a')} = \frac{1-a}{(1+a')\lambda_r}. \quad [1]$$

However, if the blade motion is significant we must include the local velocities in the calculation of the inflow angle, as follows:

$$\tan \varphi = \frac{U_\infty(1-a) + v_{e-op}}{\Omega r(1+a') + v_{e-ip}}. \quad [2]$$

This equation holds for all elements of the blade along the span, although typically the inflow angle changes with element location.

The induced velocity components in Equations 1 and 2 are a function of the forces on the blades and we use BEM theory to calculate them. A thorough derivation of these equations can be found in most wind turbine design handbooks (Manwell et al. 2002; Burton et al. 2001), and so it will only be summarized here. From blade element theory and Figure 3, the thrust distributed around an annulus of width dr (see Figure 1) is equivalent to

$$dT = B \frac{1}{2} \rho V_{total}^2 (C_l \cos \varphi + C_d \sin \varphi) c dr, \quad [3]$$

and the torque produced by the blade elements in the annulus is equivalent to

$$dQ = B \frac{1}{2} \rho V_{total}^2 (C_l \sin \varphi - C_d \cos \varphi) c r dr. \quad [4]$$

Now, to relate the induced velocities in the rotor plane to the elemental forces of Equations 3 and 4 we must incorporate the momentum part of the theory, which states that the thrust extracted by each rotor annulus is equivalent to

$$dT = 4\pi r \rho U_\infty^2 (1-a) a dr, \quad [5]$$

and the torque extracted from each annular section is equivalent to

$$dQ = 4\pi r^3 \rho U_\infty \Omega (1-a) a' dr. \quad [6]$$

Thus, when we include two-dimensional airfoil tables of lift and drag coefficient as a function of the angle of attack, α , we have a set of equations that can be iteratively solved for the induced velocities and the forces on each blade element. However, before we solve our system of equations, we would like to take into account several corrections to the BEM theory. These corrections include tip- and hub-loss models to account for vortices shed at these locations, the Glauert correction to account for large induced velocities ($a > 0.4$), and the skewed wake correction to model the effects of incoming flow that is not perpendicular to the rotor plane. Each of these will be described in a section below.

Note that Equations 1-6 do not include terms for coning angle or teeter angle of the rotor plane. AeroDyn assumes that the built-in

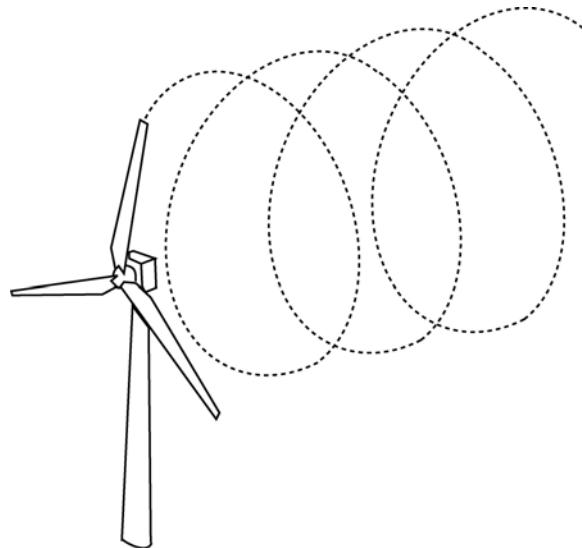


Figure 4. Helical wake pattern of single tip vortex

coning, effective coning of the rotor blades from large aeroelastic deflections, and teeter do not significantly change the aerodynamics of the rotor in operation. This assumption is tenuous, particularly for large deflection angles that will change the shape of the wake by introducing an effective skew angle. Because of this concern, the effective coning and teeter may be introduced in a future version of the code.

Tip-Loss Model

One of the major limitations of the original blade element momentum theory is that there is no influence of vortices shed from the blade tips into the wake on the induced velocity field. These tip vortices create multiple helical structures in the wake, as seen in Figure 4, and they play a major role in the induced velocity distribution at the rotor. The effect on induced velocity in the rotor plane is most pronounced near the tips of the blades, an area that also has the greatest influence on the power produced by the turbine. To compensate for this deficiency in BEM theory, AeroDyn uses a theory originally developed by Prandtl (see Glauert 1935). Prandtl simplified the wake of the turbine by modeling the helical vortex wake pattern as vortex sheets that are convected by the mean flow and have no direct effect on the wake itself. This theory is summarized by a correction factor to the induced velocity field, F , and can be expressed simply by the following:

$$F = \frac{2}{\pi} \cos^{-1} e^{-f}, \quad [7]$$

where,

$$f = \frac{B}{2} \left(\frac{R-r}{r \sin \phi} \right). \quad [8]^1$$

This correction factor is used to modify the momentum part of the blade element momentum equations, replacing Equations 5 and 6 with the following:

$$dT = 4\pi r \rho U_\infty^2 (1-a) a F dr \quad [9]$$

$$dQ = 4\pi r^3 \rho U_\infty \Omega (1-a) a' F dr. \quad [10]$$

Because of its reasonable accuracy for most operating conditions and easy formulaic implementation, the Prandtl model is often used in engineering codes such as AeroDyn. However, like most engineering models it has limitations that affect its accuracy. One limitation of this model is that it assumes the wake does not expand, limiting its validity to lightly loaded rotors. Also, Glauert (1935) showed that the accuracy, relative to the more accurate and computationally expensive Goldstein solution (1929), of this model decreases with lower numbers of blades (less than three) and higher tip speed ratios.

Figure 5 is an example of the radial distribution of the tip-loss correction for a blade that is operating such that the inflow angle, ϕ , is constant along the span at 10° . When the tip-loss model is employed, the tip-loss factor sharply decreases as the radial position along the blade approaches the blade tip. This corresponds to a dramatic increase in the induction factor near the

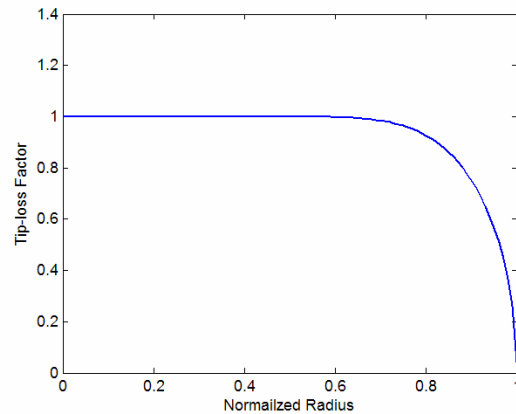


Figure 5. Tip-loss factor for blade with constant 10° inflow angle along span (optimal twist)

¹ Prandtl's original tip-loss model was based on the inflow angle at the blade tip, ϕ_{tip} . He later revised this (Glauert 1935) to the local inflow angle, making the calculation easier to implement with minimal loss in accuracy.

tip. As the induction factor increases, the resultant relative wind speed for a given blade segment decreases along with the angle of attack (see Figure 2). As a result, the loading (lift and drag forces) decreases near the tip.

In addition to the Prandtl model, users of AeroDyn also have the option of using an empirical relationship for the tip loss based on the Navier-Stokes solutions of Xu and Sankar (2002) as described in the following equations:

$$F_{new} = \frac{F_{Prandtl}^{0.85} + 0.5}{2} \quad \text{for } 0.7 \leq r/R \leq 1, \quad [11]$$

or

$$F_{new} = 1 - \left(\frac{r}{R} \right) \frac{1 - F_{Prandtl}(r/R=0.7)}{0.7} \quad \text{for } r/R < 0.7. \quad [12]$$

These relationships are a correction for the Prandtl model and must be used in conjunction with Equations 7 and 8. Note, however, that this correction was based on a specific turbine design (UAE Phase 6, Hand et al. 2001) at one wind speed and may not be applicable to all turbine configurations. It also results in a tip-loss factor greater than zero at the tip, which is physically unrealistic at the tip blade station.

Hub-Loss Model

Much like the tip-loss model, the hub-loss model serves to correct the induced velocity resulting from a vortex being shed near the hub of the rotor. The hub-loss model uses a nearly identical implementation of the Prandtl tip-loss model to describe the effect of this vortex, replacing Equation 8 with the following:

$$f = \frac{B}{2} \left(\frac{r - R_{hub}}{R_{hub} \sin \varphi} \right). \quad [13]$$

For a given element, the local aerodynamics may be affected by both the tip loss and hub loss, in which case the tip-loss and hub-loss correction factors are multiplied to create the total loss factor used in Equations 9 and 10.

Glauert Correction

Another limitation of the BEM theory is that when the induction factor is greater than about 0.4, the basic theory becomes invalid. This occurs with turbines operating at high tip speed ratios (e.g. constant speed turbine at low wind speeds), as the rotor enters what is known as the *turbulent wake state* ($a > 0.5$). According to momentum theory, this operating state results when some of the flow in the far wake starts to propagate upstream, which is a violation of the basic assumptions of BEM theory. Physically, this flow reversal cannot occur, and what actually happens is more flow entrains from outside the wake and the turbulence increases. The flow behind the rotor slows down, but the thrust on the rotor disk continues to increase. To compensate for this effect, Glauert (1926) developed a correction to the rotor thrust coefficient based on experimental measurements of helicopter rotors with large induced velocities. While this model was originally developed as a correction to the thrust coefficient of an entire rotor, it has also been used to correct the local coefficient of the individual blade elements when used with BEM theory. Because of this, it is important to understand the Glauert correction's

relationship to the tip-loss model. When the losses near the tip are high, the induced velocities are large; therefore, the possibility of a turbulent wake near the tips increases. Thus, for each element the total induced velocity calculation must use a combination of the tip-loss and Glauert corrections. Buhl (2004) derived a modification to the Glauert empirical relation that included the tip-loss correction as follows:

$$C_T = \frac{8}{9} + (4F - \frac{40}{9})a + (\frac{50}{9} - 4F)a^2, \quad [14]$$

or, solving for the induction factor,

$$a = \frac{18F - 20 - 3\sqrt{C_T(50 - 36F) + 12F(3F - 4)}}{36F - 50}. \quad [15]$$

This empirical relationship is different from those in the models of other authors (Manwell 2002; Burton 2001). But, this relationship is necessary to eliminate a numerical instability when using the Glauert correction to calculate the elemental thrust in conjunction with the tip-loss correction

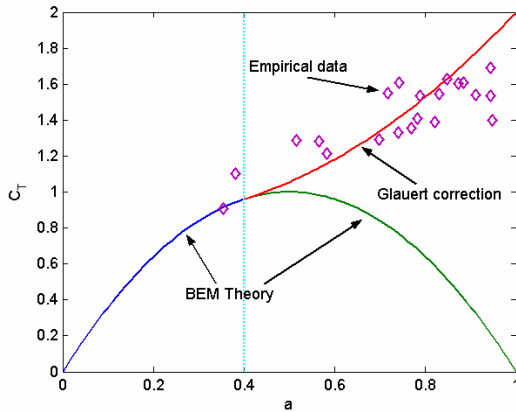


Figure 6. Glauert correction for tip-loss factor, $F = 1.0$

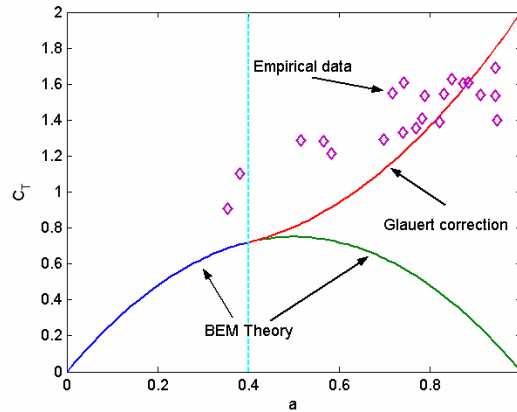


Figure 7. Glauert correction for tip-loss factor, $F = 0.75$

model.

Figure 6 shows an example of the Glauert correction when the tip-loss factor is equal to one. When the induction factor, a , is 0.4 the BEM theory and Glauert correction produce the same value for thrust coefficient of 0.96. The slopes are also equivalent at this induction factor. When the tip-loss factor is less than one (e.g. 0.75, as in Figure 7), the BEM theory predicts a much lower thrust coefficient for most induction factors. Thus, to prevent numerical instability in AeroDyn, the Glauert correction must also adjust so that the value and slopes again match at the induction factor of 0.4. This figure demonstrates the sensitivity of the induction factor to the tip-loss factor seen in Equation 15.

Again, note that the Glauert correction was developed as a correction to an entire rotor disk; the original researchers did not intend it to be applied to a rotor annulus. However, because of a limited amount of experimental data, an alternative model with BEM theory does not currently exist.

Skewed Wake Correction

Another disadvantage of blade element momentum theory is that it was originally designed for axisymmetric flow. Often, however, wind turbines operate at yaw angles relative to the incoming

wind, which produces a skewed wake behind the rotor. The BEM model needs to be corrected to account for this skewed wake effect. The formulation used in AeroDyn is based on an equation originally developed by Glauert (1926) who was primarily interested in the autogyro. The basic formula of the skewed wake correction he derived is

$$a_{skew} = a \left[1 + K \frac{r}{R} \cos \psi \right], \quad [16]$$

where the constant K is a function of the skew angle.

Many skewed wake correction models are derived from this formulation. The one implemented in AeroDyn is based on a method developed by Pitt and Peters (1981) (see also Snel and Schepers 1995). Assuming steady inflow conditions, the skewed wake formulation is

$$a_{skew} = a \left[1 + \frac{15\pi}{32} \frac{r}{R} \tan \frac{\chi}{2} \cos \psi \right], \quad [17]$$

where ψ is defined as the azimuth angle that is zero at the most downwind position of the rotor plane, after accounting for both tilt and yaw (see Figure 8). This position has the greatest amount of induced velocity, whereas the most upwind position ($\cos \psi = -1$) has the least induced velocity.

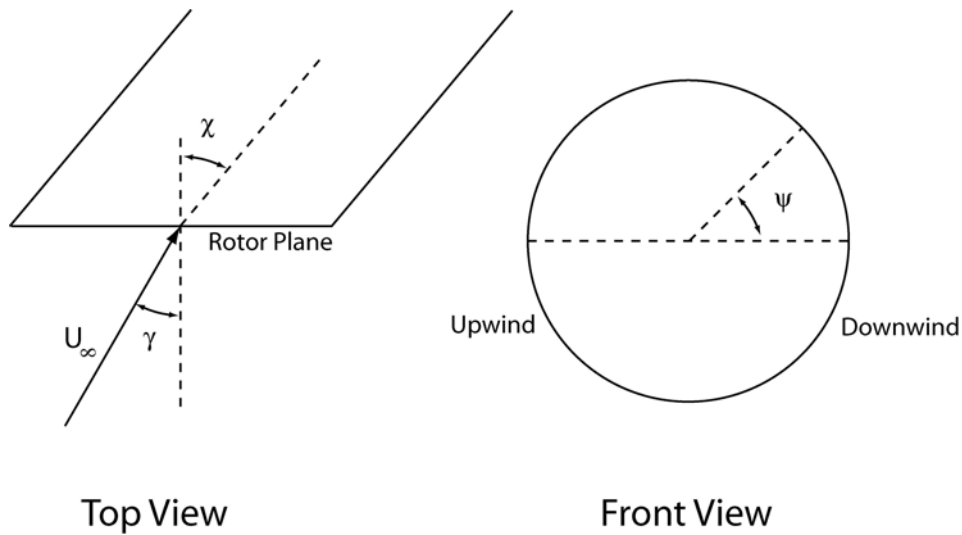


Figure 8. Coordinates used in skewed wake correction

Although Glauert's model originally assumed a was the induced velocity for the entire rotor, AeroDyn uses this correction for each element. Therefore, a and a_{skew} apply to the local elemental induced velocities.

Notice that the constant K in Equation 16 is a function of the wake skew angle, χ , rather than the rotor yaw angle, γ . The wake angle is the actual flow angle leaving the turbine and is slightly larger than the skew angle, which is defined as the difference between the incoming flow and rotor plane, as seen in Figure 8. Using the analysis of Coleman et al. (1945), we can relate the wake skew angle to the yaw angle in the following formula:

$$\tan \chi = \frac{U_{\infty} (\sin \gamma - a \tan \frac{\chi}{2})}{U_{\infty} (\cos \gamma - a)}, \quad [18]$$

which can be approximated by the following relationship according to Burton et al. (2001):

$$\chi = (0.6a + 1)\gamma. \quad [19]$$

As with previous models, the skewed wake correction has limitations. The major limitation of this model is that it assumes a cylindrical wake, which is valid only for lightly loaded rotors. Also, there is no firm theoretical basis for applying this correction to BEM theory, even though it has improved results for predicting yaw moments and motions when compared with those of the standard theory (Hansen 1992; Snel and Schepers 1995). In addition, recent research has found that this correction may be too large in some situations (see Eggers et al. 2000). We believe that, for wind turbines consistently operating in yaw, the generalized dynamic wake model described below is a better alternative for making more accurate predictions of the turbine aerodynamics.

Other Corrections

Previous researchers (Wilson and Patton 1978) have suggested various other corrections to the BEM theory. These corrections include accounting for the blade thickness effect on local angle of attack, cascade width for high solidity turbines, and spanwise gaps for partial span pitch control. Blade thickness and cascade effects can be aerodynamically significant near the rotor hub and may affect the in-plane yaw forces on the rotor. At this time, AeroDyn does not model these effects, but future research may necessitate adding these corrections at some later time. Spanwise gaps are not modeled in AeroDyn because partial span pitch control is not used in most modern turbine designs.

Final Iteration Procedure for Blade Element Momentum Theory

Now that all of the equations for BEM theory have been established, we will identify the iteration procedure used in AeroDyn to calculate the induced velocities, angles of attack, and thrust coefficients for each blade element along the span of a blade. To begin the calculation we must first estimate the axial induction factor. One efficient way to do this is to use Equations 21 and 27 below, assume that the inflow angle φ is small ($\sin\varphi \approx \varphi$), the tangential induction a' is zero, the tip and hub-loss corrections F are one, the drag coefficient C_d is zero, the lift coefficient, $C_l = 2\pi\alpha$, and finally, $\alpha = \varphi - \beta$. After some rearranging, we arrive at the initial estimate of the axial induction factor:

$$a = \frac{1}{4} \left[2 + \pi\lambda_r\sigma' - \sqrt{4 - 4\pi\lambda_r\sigma' + \pi\lambda_r^2\sigma'(8\beta + \pi\sigma')} \right]. \quad [20]$$

From here we can estimate the inflow angle using an initial assumption of zero for the tangential induction, a' and

$$\tan\varphi = \frac{U_\infty(1-a) + v_{e-op}}{\Omega r(1+a') + v_{e-ip}}. \quad [21]$$

Next, AeroDyn determines the thrust coefficient for the element using the following:

$$C_T = \frac{\sigma'(1-a)^2(C_l \cos\varphi + C_d \sin\varphi)}{\sin^2\varphi}. \quad [22]$$

Then, the tip- and hub-loss corrections are calculated as follows:

$$F_{tip} = \frac{2}{\pi} \cos^{-1} e^{-\left(\frac{B(R-r)}{2r\sin\varphi}\right)} \quad [23]$$

$$F_{hub} = \frac{2}{\pi} \cos^{-1} e^{-\left(\frac{B(r-R_{hub})}{2R_{hub} \sin \varphi}\right)} \quad [24]$$

$$F = F_{hub} F_{tip}. \quad [25]$$

Now, if $C_T > 0.96F$, the element is highly loaded and the modified Glauert correction will be used to determine the new axial induction factor:

$$a = \frac{18F - 20 - 3\sqrt{C_T(50 - 36F) + 12F(3F - 4)}}{36F - 50}. \quad [26]$$

If $C_T \leq 0.96F$, the standard BEM theory is used to calculate the axial induction:

$$a = \left[1 + \frac{4F \sin^2 \varphi}{\sigma'(C_l \cos \varphi + C_d \sin \varphi)} \right]^{-1}. \quad [27]$$

The tangential induction factor is calculated using

$$a' = \left[-1 + \frac{4F \sin \varphi \cos \varphi}{\sigma'(C_l \sin \varphi - C_d \cos \varphi)} \right]^{-1}. \quad [28]$$

And finally, the effect of skew is included using the skewed wake correction factor:

$$a_{skew} = a \left[1 + \frac{15\pi}{32} \frac{r}{R} \tan \frac{\chi}{2} \cos \psi \right]. \quad [29]$$

This process is then repeated for each element, starting again with Equation 21 and iterated until the values of induction factors and inflow angle have converged to their final values.

In AeroDyn, the user has some control over how the induced velocities are calculated. Four of the options in the calculation routine are (1) whether to include drag in the induction calculations (axial or tangential), (2) whether to include tip losses, (3) whether to include hub losses, and (4) whether to calculate rotational induction. If the user chooses not to include drag in the induction calculation (as recommended by Wilson and Lissaman 1974) the C_d term in the above equations is set to zero. Similarly, if the tangential induction is neglected, AeroDyn will ignore Equation 28 and assume all induction is in the axial direction. Finally, if both tip and hub losses are ignored, the parameter F will be set to one for all of the above equations. If tip losses are desired but not hub losses, the parameter F will be calculated only near the tip, and likewise when only hub losses are modeled.

Currently in AeroDyn, these equations are not directly coupled with the dynamic stall routines explained below. In this iteration process, only static coefficients of lift and drag are used to calculate the properties of the wake. Once all of the induced velocities and angles of attack are calculated, the dynamic stall routines are called and the forces returned to the aeroelastic code are calculated. This decoupling was assumed for two reasons. First, the wake cannot fully respond to short-term dynamic stall events, so they should not always affect the wake. Second, the code is faster and simpler without this coupling. However, some dynamic stall events such as those due to persistent skewed flow can affect the entire wake, so this assumption is not always valid. The decoupling should be refined after future research. This is another reason that the blade element momentum method is not preferred for unsteady or highly skewed flows.

Generalized Dynamic Wake

The generalized dynamic wake (GDW) model of AeroDyn is based on the work of Peters and He (1989) and was implemented in the code by Suzuki (2000) for his Ph.D. thesis at the University of Utah. This model was originally developed for the helicopter industry, and it is also known as the *acceleration potential method*. An advantage of this method is that it allows for a more general distribution of pressure across a rotor plane than BEM theory. It is an extension of the often-used Pitt and Peters (1981) model, with more flow states and a fully nonlinear implementation to account for turbulence and spatial variation of the inflow.

The GDW method is based on a potential flow solution to Laplace's equation. Kinner (1937) used this solution to develop the equations for the pressure distributions in the rotor plane, which consist of an infinite series of Legendre functions in the radial direction and trigonometric functions in the azimuthal direction. In his derivation, Kinner started from the Euler equations (inviscid and incompressible flow), assumed that the induced velocities were small in comparison to the mean wind speed and regarded the rotor as an infinite number of slender blades, to keep the solidity low.

The main advantages of the generalized dynamic wake method over blade element momentum theory include inherent modeling of the dynamic wake effect, tip losses, and skewed wake aerodynamics. The dynamic wake effect is the time lag in the induced velocities created by vorticity being shed from the blades and being convected downstream. Figure 9 contains an example of the time lag effect on the power output of a turbine. It shows the measured power output of the Tjæreborg turbine (Suzuki 2000) operating in a 10.6 m/s mean wind. During a 60 second period, the turbine blades were pitched from 0.2° to 3.9° over a period of 1.0 seconds and then back to 0.2° again. After each blade pitch change, the power changes quickly resulting in an overshoot and then gradually returns to a new equilibrium value over the next 25+ seconds. Also in the figure are predictions of this event using both BEM and GDW theory. Notice that the BEM theory has no time lag, but the GDW does. However, the time constant is shorter than that exhibited by the data in the figure. The small oscillations in the BEM prediction are due to structural vibrations and not the aerodynamic model itself. We estimate that similar amplitude structural oscillations also appear in the GDW model. Therefore, most of the overshoot seen in Figure 9 is due to the aerodynamic time lag predicted by the model. This time lag is longer than that experienced by helicopters and was calibrated to typical wind turbine response times using experimental data in Suzuki's thesis (2000).

Another advantage of this method is that the induced velocities in the rotor plane are determined from a set of first-order differential equations, which can be solved using a non-iterative technique. The technique used in AeroDyn is the fourth-order Adams-Bashford-Moulton (Press et al. 1982) predictor-corrector method. Because iteration is not required, the model can also be directly incorporated with a dynamic stall model for determining the aerodynamic coefficients of each blade element. Although, as currently written, AeroDyn determines the dynamic stall effects after the GDW equations have been solved.

Like the BEM theory, the GDW method has its limitations. As with most wake models, the generalized dynamic wake was developed for lightly loaded rotors and assumes that the induced velocities are small relative to the mean flow. This basic assumption leads to instability of the method at low wind speeds when the turbulent wake state is approached (Laino and Hansen, 2004). To avoid this computational instability, AeroDyn currently switches to the BEM method when the mean wind speed is below 8 m/s. Another disadvantage of the model is that it does not account for wake rotation. To correct for this, AeroDyn uses the BEM equation to calculate the tangential induction factor, as in Equation 28. Finally, the GDW method assumes that the rotor plane is a flat disk. Therefore, the effect of large aeroelastic deflections or significant coning of the rotor blades on the wake aerodynamics will not be accurately modeled.

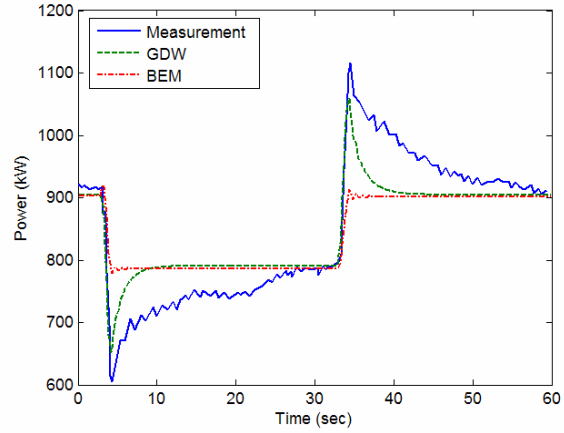


Figure 9. Generator power output during rapid pitch changes (from 0.2° to 3.9° and back) for the Tjæreborg turbine, Suzuki (2000)

Basic Derivation

The basic governing equations of the generalized dynamic wake are derived from the Euler equations. Assuming that the induced velocities are small perturbations relative to the freestream inflow, conservation of momentum simplifies to

$$\frac{\partial u_i}{\partial t} + U_{\infty j} \frac{\partial u_i}{\partial x_j} = -\frac{1}{\rho} \frac{\partial p}{\partial x_i}, \quad [30]$$

and conservation of mass resulting in

$$\frac{\partial u_i}{\partial x_i} = 0, \quad [31]$$

finally leading to Laplace's equation for the pressure distribution:

$$\nabla^2 p = 0. \quad [32]$$

It is convenient to non-dimensionalize these equations with the rotor tip speed, which is a widely used convention in rotorcraft aerodynamics, and also the hub-height wind speed, which is common in wind turbine aerodynamics. This results in the following nondimensional quantities:

$$\text{time:} \quad \hat{t} = \Omega t \quad [33]$$

$$\text{displacements:} \quad \hat{x}_i = \frac{x_i}{R} \quad [34]$$

$$\text{velocities:} \quad \hat{u}_i = \frac{u_i}{\Omega R} \text{ and } \hat{U}_{\infty} = \frac{U_{\infty}}{\Omega R} \quad [35]$$

$$\text{pressure:} \quad \Phi = \frac{p}{\rho \cdot (\Omega R)^2} \quad [36]$$

Note that most of these dimensionless variables are dependent on the rotor speed, Ω . Because the rotor speed may change over the course of a simulation (e.g. a variable speed turbine), these quantities must be calculated at the beginning of each time step.

The two primary equations for the generalized dynamic wake are then made dimensionless. Laplace's equation (Equation 32) is also true for the dimensionless pressure:

$$\nabla^2 \Phi = 0, \quad [37]$$

and the momentum equation becomes

$$\frac{\partial \hat{u}_i}{\partial \hat{t}} + \hat{U}_{\infty j} \frac{\partial \hat{u}_i}{\partial \hat{x}_j} = -\frac{\partial \Phi}{\partial \hat{x}_i}. \quad [38]$$

The boundary conditions for these differential equations are given by the aerodynamic loading on the rotor blades and the requirement that the pressure return to ambient pressure far from the rotor. Also, the pressure discontinuity across the rotor plane must apply a force equal to the rotor thrust.

Using linear superposition, the pressure field can be divided into two components: one modeling the spatial variation of the pressure distribution, Φ^V , and one modeling the unsteadiness, Φ^A , where:

$$\Phi = \Phi^V + \Phi^A. \quad [39]$$

By dividing the pressure field into two components, Equation 38 can also be divided into two separate equation sets as follows:

$$\frac{\partial \hat{u}_i}{\partial \hat{t}} = -\frac{\partial \Phi^A}{\partial \hat{x}_i}, \quad [40]$$

and

$$\hat{U}_{\infty j} \frac{\partial \hat{u}_i}{\partial \hat{x}_j} = -\frac{\partial \Phi^V}{\partial \hat{x}_i}. \quad [41]$$

Assuming that the differential equations (Equations 40 and 41) are linear and can be represented by a set of operators L and E , the equations become:

$$\frac{\partial \hat{u}_i}{\partial \hat{t}} = \hat{u}_i^* = L[\Phi^A], \quad [42]$$

and

$$\hat{u}_i = L[\Phi^V]. \quad [43]$$

As long as the operators L and E are invertible the solution for the dimensionless pressure field is

$$\Phi = \Phi^V + \Phi^A = L^{-1}[\hat{u}] + E^{-1}[\hat{u}]^*. \quad [44]$$

If an operator M is defined as the inverse of E , Equation 44 becomes,

$$M[\hat{u}]^* + L^{-1}[\hat{u}] = \Phi. \quad [45]$$

This is the general form of the governing equation of the generalized dynamic wake model that relates the induced velocity to the pressure field on the rotor disk. The methods used to solve these equations are described below.

Pressure Distribution

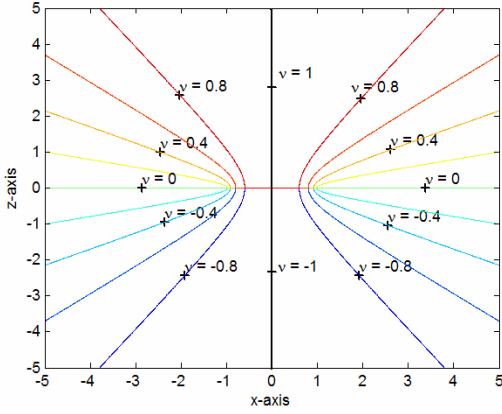


Figure 10. Contours of constant ν in the x - z plane

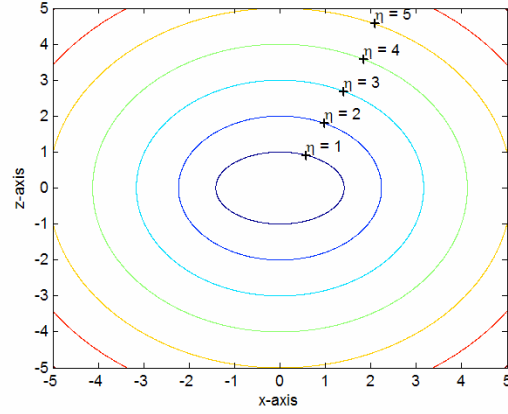


Figure 11. Contours of constant η in the x - z plane

Kinner (1937) developed the pressure distribution that satisfies Laplace's equation (Equation 37) and that gives pressure discontinuity across a circular disk (the rotor). This solution was originally developed for the problem of a circular wing, but with different boundary conditions, also applies to a yawed actuator disk. The pressure distribution is given in an ellipsoidal coordinate system.

$$\Phi(\nu, \eta, \psi, \hat{t}) = \sum_{m=0}^{\infty} \sum_{n=m+1, m+3, \dots}^{\infty} P_n^m(\nu) Q_n^m(i\eta) [C_n^m(\hat{t}) \cos(m\psi) + D_n^m(\hat{t}) \sin(m\psi)], \quad [46]$$

where and ν , η and ψ are ellipsoidal coordinates defined by the following relationships:

$$x = \sqrt{1 - \nu^2} \sqrt{1 + \eta^2} \cos \psi \quad [47]$$

$$y = \sqrt{1 - \nu^2} \sqrt{1 + \eta^2} \sin \psi \quad [48]$$

$$z = \nu \eta. \quad [49]$$

Note that this xyz coordinate system follows the convention of the helicopter industry, with the x - y plane parallel with the rotor plane, and the positive- z -axis perpendicular to the rotor plane in the upwind direction (see Figure 12). Also, note that the relationship between the dimensionless radius, \hat{r} , and ν in the ellipsoidal coordinate is given as $\hat{r} = \sqrt{1 - \nu^2}$.

The ν - η - ψ coordinate system covers the entire three-dimensional space once and only once, if ν , η , and ψ are restricted to the ranges

$$-1 \leq \nu \leq 1 \quad [50]$$

$$0 \leq \eta \leq \infty \quad [51]$$

$$0 \leq \psi \leq 2\pi. \quad [52]$$

Figures 10 and 11 show contours of constant ν and η , respectively, in the x - z plane (perpendicular to the rotor plane). The constant ν surfaces are hyperboloids and the constant η surfaces are ellipsoids. Both families of surfaces are azimuthally symmetric about the z -axis. The coordinate ψ is the azimuthal angle measured from the positive x -axis and is positive in the clockwise direction. The $\eta = 0$ surface represents both sides of the disk surface.

The pressure field of Equation 46 is discontinuous only within the unit circle (the rotor), where

$\eta = 0$. And, because the pressure is perfectly continuous outside of the rotor, this distribution satisfies one of the boundary conditions that the rotor thrust force is zero outside the rotor boundary.

This pressure discontinuity provides thrust force on the rotor that simulates the aerodynamic forces on the blades. Although the actual aerodynamic forces act only on the blades and are discretely distributed, the distribution in Equation 46 gives a continuous distribution. However, the distribution starts to have peaks at the blades and to show the characteristics of discontinuity, as the number of terms of the series solution (flow states) increases.

The rotor disk pressure loading can be obtained as the pressure difference between the upwind and downwind surfaces of the rotor plane (He 1989),

$$P(\hat{r}, \psi, \hat{t}) = -2 \sum_{m=0}^{\infty} \sum_{n=m+1, m+3, \dots}^{\infty} P_n^m(\nu) Q_n^m(i0) [C_n^m(\hat{t}) \cos(m\psi) + D_n^m(\hat{t}) \sin(m\psi)], \quad [53]$$

or,

$$P(\hat{r}, \psi, \hat{t}) = \sum_{m=0}^{\infty} \sum_{n=m+1, m+3, \dots}^{\infty} \hat{P}_n^m(\nu) [\tau_n^{mc}(\hat{t}) \cos(m\psi) + \tau_n^{ms}(\hat{t}) \sin(m\psi)], \quad [54]$$

where

$$\hat{P}_n^m(\nu) = (-1)^m \frac{P_n^m(\nu)}{\rho_n^m} \quad [55]$$

$$(\rho_n^m)^2 = \frac{1}{2n+1} \frac{(n+m)!}{(n-m)!} \quad [56]$$

$$\tau_n^{mc} = (-1)^{m+1} 2Q_n^m(i0) \rho_n^m C_n^m \quad [57]$$

$$\tau_n^{ms} = (-1)^{m+1} 2Q_n^m(i0) \rho_n^m D_n^m. \quad [58]$$

The dimensionless pressure quantities, τ_n^{mc} and τ_n^{ms} , couple the pressure distribution to the forces on the blades, as explained below.

The term $\hat{P}_n^m(\nu)$ is called the “normalized” associated Legendre function of the first kind, since it satisfies

$$\int_0^1 [\hat{P}_n^m(\nu)]^2 d\nu = 1 \quad [59]$$

Induced Velocity Distribution

Similar to the expansion of the pressure distribution, the induced velocity distribution (the component normal to the rotor plane) can be expressed as an infinite series as shown in Equation 60 (He 1989):

$$\hat{u}(\hat{r}, \psi, \hat{t}) = \sum_{r=0}^{\infty} \sum_{j=r+1, r+3, \dots}^{\infty} \phi_j^r(\nu) [\alpha_j^r(\hat{t}) \cos(r\psi) + \beta_j^r(\hat{t}) \sin(r\psi)], \quad [60]$$

where the radial shape functions, $\phi_j^r(\nu)$, are linearly independent and complete for a given harmonic, r . The coefficients α_j^r and β_j^r can be regarded as the time-dependent states of the

induced-velocity field. The shape functions are defined as

$$\phi_j^r(\hat{r}) = \sqrt{(2j+1)H_j^r} \sum_{q=r, r+2, \dots}^{j-1} \hat{r}^q \frac{(-1)^{\frac{q-r}{2}} (j+q)!!}{(q-r)!!(q+r)!!(j-q-1)!!} \quad [61]$$

$$H_j^r = \frac{(j+r-1)!!(j-r-1)!!}{(j+r)!!(j-r)!!} \quad [62]$$

$n!!$ is a double factorial, defined as

$$n!! \equiv \begin{cases} n \cdot (n-2) \cdot (n-4) \cdots 3 \cdot 1 & (n = \text{odd}) \\ n \cdot (n-2) \cdot (n-4) \cdots 4 \cdot 2 & (n = \text{even}) \end{cases} \quad [63]$$

For example, the first four shape functions of $r = 2$ are

$$\phi_1^0(\hat{r}) = \sqrt{3} \quad [64]$$

$$\phi_3^0(\hat{r}) = \sqrt{7} - \frac{5\sqrt{7}}{2} \hat{r}^2 \quad [65]$$

$$\phi_2^1(\hat{r}) = \sqrt{\frac{15}{2}} \hat{r} \quad [66]$$

$$\phi_3^2(\hat{r}) = \frac{\sqrt{210}}{4} \hat{r}^2 \quad [67]$$

Expansion of Governing Equation

With both the dimensionless pressure at the rotor disk and the induced velocity distribution expressed as infinite series of sines and cosines, they can be combined into the governing equation (45) (He 1989). The two operators are represented by square matrices.

The pressure coefficients in Equation 54, τ_n^{mc} and τ_n^{ms} , and the velocity coefficients in Equation 60, α_j^r and β_j^r , have a relationship shown in Equations 68 and 69, which separate the cosine terms and sine terms. Equation 68 is the governing equation for the cosine terms and Equation 69 is the governing equation for the sine terms.

$$[M^c] \begin{Bmatrix} \vdots \\ \alpha_j^r \\ \vdots \end{Bmatrix}^* + [L^c]^{-1} \begin{Bmatrix} \vdots \\ \alpha_j^r \\ \vdots \end{Bmatrix} = \frac{1}{2} \begin{Bmatrix} \vdots \\ \tau_n^{mc} \\ \vdots \end{Bmatrix} \quad [68]$$

$$[M^s] \begin{Bmatrix} \vdots \\ \beta_j^r \\ \vdots \end{Bmatrix}^* + [L^s]^{-1} \begin{Bmatrix} \vdots \\ \beta_j^r \\ \vdots \end{Bmatrix} = \frac{1}{2} \begin{Bmatrix} \vdots \\ \tau_n^{ms} \\ \vdots \end{Bmatrix} \quad [69]$$

where $[M^c]$ and $[M^s]$ are the cosine and sine terms of the M-operator (see Equation 45) and similarly with the $[L^c]$ and $[L^s]$ matrices. The M-operator (apparent mass matrix) is nearly identical for both of the cosine and sine equations, with the exception that $[M^c]$ has elements for $m = 0$ and $[M^s]$ does not. The M-operators for both sine and cosine terms are given as

$$[M] = \begin{bmatrix} \ddots & & & \\ & \ddots & & \\ & & K_n^m & \\ & & & \ddots \end{bmatrix} \quad [70]$$

$$K_n^m = \frac{2}{\pi} H_n^m = \frac{2}{\pi} \frac{(n+m-1)!!(n-m-1)!!}{(n+m)!!(n-m)!!} \quad [71]$$

This mass matrix is purely diagonal, indicating that there is no coupling in either the harmonic or radial direction. This diagonal structure also simplifies the computation in a time marching scheme.

The L-operator (inflow gain matrix) is different for the sine and cosine equations and can be divided into matrices dependent on the flow parameters, $[\hat{V}]$, and the wake skew angle, $[\tilde{L}]$, as follows:

$$[L^c]^{-1} = [\tilde{L}^c]^{-1} [\hat{V}^c] \quad [72]$$

$$[L^s]^{-1} = [\tilde{L}^s]^{-1} [\hat{V}^s]. \quad [73]$$

The matrices dependent on wake skew angle can be expressed as

$$[\tilde{L}_{jn}^{om}]^c = X^m [\Gamma_{jn}^{om}] \quad [74]$$

$$[\tilde{L}_{jn}^{rm}]^c = [X^{|m-r|} + (-1)^l X^{|m+r|}] [\Gamma_{jn}^{rm}] \quad [75]$$

$$[\tilde{L}_{jn}^{rm}]^s = [X^{|m-r|} - (-1)^l X^{|m+r|}] [\Gamma_{jn}^{rm}] \quad [76]$$

with

$$l = \min(r, m) \quad [77]$$

$$X = \tan \left| \frac{\chi}{2} \right| = \frac{\mu}{V_T + |\lambda|} \quad (0 \leq \chi \leq \pi/2) \quad [78]$$

$$\Gamma_{jn}^{rm} = \frac{(-1)^{\frac{n+j-2r}{2}}}{\sqrt{H_n^m H_j^r}} \frac{2\sqrt{(2n+1)(2j+1)}}{(j+n)(j+n+2)[(j-n)^2 - 1]}, \quad \text{for } r+m = \text{even} \quad [79]$$

$$\Gamma_{jn}^{rm} = \frac{\pi}{2\sqrt{H_n^m H_j^r}} \frac{\text{sign}(r-m)}{\sqrt{(2n+1)(2j+1)}}, \quad \text{for } r+m = \text{odd and } |j-n| = 1 \quad [80]$$

$$\Gamma_{jn}^{rm} = 0, \quad \text{for } r+m = \text{odd and } |j-n| \neq 1. \quad [81]$$

Note that the wake angle function of Equation 78 is determined from the average wake angle using the flow parameters described below. Also, the terms X^m and $X^{|m-r|}$, in Equations 74 - 76, can become 0^0 . This zero raised to the zeroth power is considered one.

As with the M-operator the matrices dependent on flow parameters, $[\hat{V}]$, are nearly identical for both of the cosine and sine equations, with the exception of $m = 0$ as follows:

$$[\hat{V}^c] = \begin{bmatrix} \ddots & & & \\ & \ddots & & \\ & & \hat{V}_n^m & \\ & & & \ddots \end{bmatrix} \text{ for } m = 0, 1, 2, 3, \dots \quad [82]$$

$$[\hat{V}^s] = \begin{bmatrix} \ddots & & \\ & \hat{V}_n^m & \\ & & \ddots \end{bmatrix} \text{ for } m = 1, 2, 3, \dots \quad [83]$$

where

$$\hat{V}_1^0 = V_T \text{ for } (m, n) = (0, 1) \quad [84]$$

$$\hat{V}_n^m = V \text{ for } (m, n) \neq (0, 1). \quad [85]$$

The flow parameters of Equations 84 and 85 are based on the inflow (including blade motion) and induced velocities described in the next section.

Flow Parameters

The inflow parameter, V , accounts for the energy that the rotor subtracts from the flow. It is calculated as follows (He 1989):

$$V = \frac{\mu^2 + (\lambda + \lambda_m)\lambda}{\sqrt{\mu^2 + \lambda^2}} \quad [86]$$

and the total flow parameter

$$V_T = \sqrt{\mu^2 + \lambda^2}. \quad [87]$$

where μ is the advance ratio (in-plane velocity divided by tip speed), and the induced velocities, λ , are found by

$$\lambda = \lambda_m + \lambda_f \quad [88]$$

$$\lambda_f = \frac{U_\infty \cos \chi}{\Omega R} \quad [89]$$

And λ_m is calculated using Equation 90:

$$\lambda_m = \sqrt{3}\alpha_1^0. \quad [90]$$

The directions of each of these quantities are shown in Figure 12. Again, the wake skew angle, χ , of Equation 89 is the average over the entire rotor. The coupling between V_T and α_1^0 makes the theory nonlinear.

Pressure Coefficients

The pressure coefficients, τ_n^{mc} and τ_n^{ms} , need to be coupled with the blade loading, which gives the boundary conditions of the model. Let L_i^q be equal to the aerodynamic force normal to the rotor plane acting on blade element i of blade q (the element thrust force). If this element thrust force is normalized by the thrust force from the dynamic pressure of the flow:

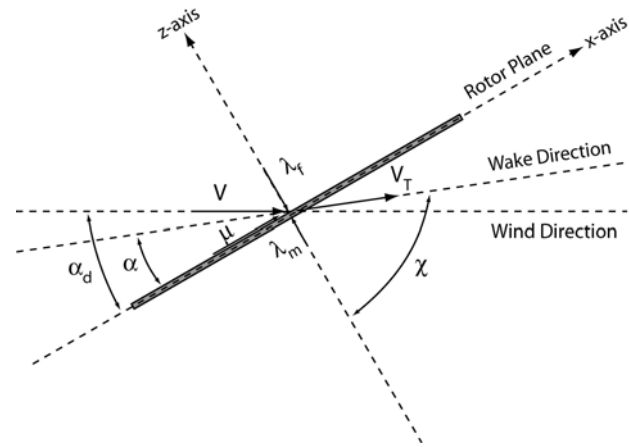


Figure 12. Velocities and coordinates used in the GDW model

$$\begin{aligned} \text{normalized element thrust force} &= \frac{L_i^q}{\rho A(\Omega R)^2} \\ &= \frac{L_i^q}{\pi \rho \Omega^2 R^4} \end{aligned} \quad [91]$$

The pressure coefficients are the normalized total thrust force multiplied by the radial expansion shape function and the azimuthal mode shape (modified from He 1989).

$$\tau_n^{mc} = \frac{1}{\pi \rho \Omega^2 R^4} \sum_{q=1}^B \left[\sum_{i=1}^{N_E} L_i^q \phi_n^m(\hat{r}_i) \right] \cos(m\psi) \quad [92]$$

$$\tau_n^{ms} = \frac{1}{\pi \rho \Omega^2 R^4} \sum_{q=1}^B \left[\sum_{i=1}^{N_E} L_i^q \phi_n^m(\hat{r}_i) \right] \sin(m\psi) \quad [93]$$

The sine terms (Equation 93) do not need to be defined for $m = 0$, because they are always multiplied by zero. The cosine terms for $m = 0$, however, need a slightly different definition because of the way $[\tilde{L}^c]$ is defined for $m=0$ in Equation 74. $[\tilde{L}^c]$ in Equation 74 is only one half of the $[\tilde{L}^c]$ in Equation 75 (modified from He, 1989). Therefore,

$$\tau_n^{0c} = \frac{1}{2\pi \rho \Omega^2 R^4} \sum_{q=1}^B \left[\sum_{i=1}^{N_E} L_i^q \phi_n^0(\hat{r}_i) \right]. \quad [94]$$

Final Governing Equations

The final set of equations for the GDW model using the parameters defined above are:

$$[M^c] \begin{Bmatrix} \vdots \\ \alpha_j^r \\ \vdots \end{Bmatrix}^* + [\tilde{L}^c]^{-1} [\hat{V}^c] \begin{Bmatrix} \vdots \\ \alpha_j^r \\ \vdots \end{Bmatrix} = \frac{1}{2} \begin{Bmatrix} \vdots \\ \tau_n^{mc} \\ \vdots \end{Bmatrix} \quad [95]$$

$$[M^s] \begin{Bmatrix} \vdots \\ \beta_j^r \\ \vdots \end{Bmatrix}^* + [\tilde{L}^s]^{-1} [\hat{V}^s] \begin{Bmatrix} \vdots \\ \beta_j^r \\ \vdots \end{Bmatrix} = \frac{1}{2} \begin{Bmatrix} \vdots \\ \tau_n^{ms} \\ \vdots \end{Bmatrix}. \quad [96]$$

The cosine term and the sine terms are not coupled. This indicates that the wake rotation is not considered in the generalized dynamic wake model itself. However, as mentioned above, AeroDyn uses the BEM method (Equation 28) to calculate the tangential components of the induced velocity. This completes the equations necessary for the generalized dynamic wake as implemented in AeroDyn.

Procedure for Generalized Dynamic Wake Calculations

The above equations are written for an infinite number of azimuthal harmonics and radial shape functions. When implemented into a computer algorithm, the number of functions used in the modeling of the pressure distribution and induced velocity field must be truncated. For the induced velocity field,

$$\hat{u}(\hat{r}, \psi, \hat{t}) = \sum_{r=0}^N \sum_{j=r+1, r+3, \dots}^{2S_r+r-1} \phi_j^r(\nu) [\alpha_j^r(\hat{t}) \cos(r\psi) + \beta_j^r(\hat{t}) \sin(r\psi)], \quad [97]$$

where N is the highest harmonic in the azimuthal direction and S_r is the number of radial shape functions for the r^{th} harmonic. The AeroDyn user must choose the values of the number of harmonics and radial shape functions to be modeled based on the structural dynamics and the desired resolution of the pressure or induced velocity distribution. The number of harmonics is often related to the number of blades. For example, He (1989) states that for a time-averaged solution of a four-bladed rotor, the induced velocity distribution can be truncated at the fourth harmonic, with little loss in accuracy. More harmonics may be required for an unsteady calculation.

Based on the number of harmonics, the number of radial shape functions can be determined. Table 1 shows the proper choice of the number of radial shape functions based on the mathematical consistency of the highest polynomial power of \hat{r} for the radial shape function at each harmonic value, m . For example, in order to truncate the induced velocity distribution at the fourth harmonic ($N = 4$) with a radial variation up to \hat{r}^8 , the number of shape functions for each harmonic is then $S_0 = 5$, $S_1 = 4$, $S_2 = 4$, $S_3 = 3$, and $S_4 = 3$. Now, remember that for $m = 0$ only one inflow state is modeled, while all other values of m model two inflow states (i.e. the sine and cosine terms of Equation 97). We can then calculate the total number of inflow states for this example, $5 + 2(4 + 4 + 3 + 3) = 33$. Whereas, if we calculate the total number of inflow states using all harmonic values for that given power of \hat{r} , we arrive at 45 inflow states, which is the last column in the table.

Table 1. Choice for the Number of Inflow Radial Shape Functions

| Highest Power of \hat{r} | m (harmonic value) | | | | | | | | | | | | | Total Inflow States |
|----------------------------|----------------------|---|---|---|---|---|---|---|---|---|----|----|----|---------------------|
| | 0 | 1 | 2 | 3 | 4 | 5 | 6 | 7 | 8 | 9 | 10 | 11 | 12 | |
| 0 | 1 | | | | | | | | | | | | | 1 |
| 1 | 1 | 1 | | | | | | | | | | | | 3 |
| 2 | 2 | 1 | 1 | | | | | | | | | | | 6 |
| 3 | 2 | 2 | 1 | 1 | | | | | | | | | | 10 |
| 4 | 3 | 2 | 2 | 1 | 1 | | | | | | | | | 15 |
| 5 | 3 | 3 | 2 | 2 | 1 | 1 | | | | | | | | 21 |
| 6 | 4 | 3 | 3 | 2 | 2 | 1 | 1 | | | | | | | 28 |
| 7 | 4 | 4 | 3 | 3 | 2 | 2 | 1 | 1 | | | | | | 36 |
| 8 | 5 | 4 | 4 | 3 | 3 | 2 | 2 | 1 | 1 | | | | | 45 |
| 9 | 5 | 5 | 4 | 4 | 3 | 3 | 2 | 2 | 1 | 1 | | | | 55 |
| 10 | 6 | 5 | 5 | 4 | 4 | 3 | 3 | 2 | 2 | 1 | 1 | | | 66 |
| 11 | 6 | 6 | 5 | 5 | 4 | 4 | 3 | 3 | 2 | 2 | 1 | 1 | | 78 |
| 12 | 7 | 6 | 6 | 5 | 5 | 4 | 4 | 3 | 3 | 2 | 2 | 1 | 1 | 91 |

Once the user determines number of inflow states, the calculation of the induced velocity proceeds as follows. Because the GDW method in AeroDyn is based on a solution of ordinary differential equations in time, it must rely on initial values of various parameters to accurately calculate the effect of the wake. The initial values are based on BEM calculations of the operating turbine over the first second of the time simulation. After one second has passed

in the simulation, AeroDyn switches from the BEM method to the GDW using the BEM solution as the initial condition for the GDW method. The blade forces are used to calculate the pressure coefficients, τ_n^{mc} and τ_n^{ms} , in Equations 91 through 94, which form the right hand side of Equations 95 and 96. Equations 92-94 transform the loading on the blades to a pressure distribution around the entire actuator disk. The apparent mass matrix, $[M]$, is calculated for each harmonic and radial shape function based on Equations 70 and 71. The inflow gain matrix, $[\tilde{L}]$, is calculated based on the wake skew angle in the formulae given in Equations 74-81. The flow parameter matrix, $[\hat{V}]$, is assembled based on formulae 82-90. Once all of the matrices are assembled, Equations 95 and 96 are solved using a fourth-order Adams-Bashford-Moulton (Press et al. 1982) predictor-corrector method, for each of the azimuthal harmonics and radial shape functions. The solutions of these equations are the coefficients of Equation 60, α_j^r and β_j^r . These coefficients are then fed back into Equation 60, along with the radial shape functions of Equations 61-63, in order to calculate the induced velocity field at any point in the rotor plane. These induced velocities are then used to determine the angle of attack for each element. This angle of attack is passed to the airfoil aerodynamics routines that return the elemental force based on either static or dynamic stall airfoil conditions as explained below. These forces are the output of the AeroDyn routines and are passed back to the aeroelastic code for further analysis. Starting at the next time step, the process is repeated using the most recent estimated forces to calculate the pressure coefficients in Equations 92 through 94, which serve as the initial conditions for Equations 95 and 96.

Airfoil Aerodynamics

The aerodynamics calculations in AeroDyn are based on the pseudo two-dimensional properties of the local airfoil aerodynamics. The term “pseudo” is used because the user can modify the airfoil properties to include three-dimensional effects such as those from aspect ratio and rotational augmentation of the rotor blades. The user has two options for calculating the airfoil aerodynamics: static airfoil tables or a dynamic stall model. If the static airfoil tables are used, the aerodynamic performance of each airfoil is simply a table lookup of the data provided in the airfoil input file. If the user selects the dynamic stall option, the static airfoil coefficients are modified as a function of angle of attack and rate of change of angle of attack, as described in the next section. No other adjustments are made to the static airfoil properties. If the user wishes to include the effects of rotational augmentation, this must be accomplished using a static airfoil data table that has been adjusted by the user.

The importance of using accurate airfoil properties cannot be overstated, nor can the difficulty of obtaining reliable data for some airfoils that are in common use. It is well established that roughness due to soiling or manufacturing, deviation of the actual section from the design shape, Reynolds number, and three-dimensional, rotating blade effects can all have a significant influence on load predictions. AeroDyn places the entire burden of obtaining reliable airfoil data upon the user. AeroDyn does some very simple bounds checking in the hope of detecting an angle of attack or coefficient that is outside a reasonable range. This may detect typographical errors, but it should not be relied on to detect inaccurate airfoil data.

It is our belief, based upon numerous model validation studies (see Simms et al. 2001 and Tangler 2002), that errors in airfoil data tables are the single largest source of error in most rotor load and performance predictions. When we "tune" a model to achieve a better match with test results, we usually make small changes in the airfoil tables (particularly near stall) and realize improvements in all predicted quantities. Unfortunately, we are not aware of a consistent method

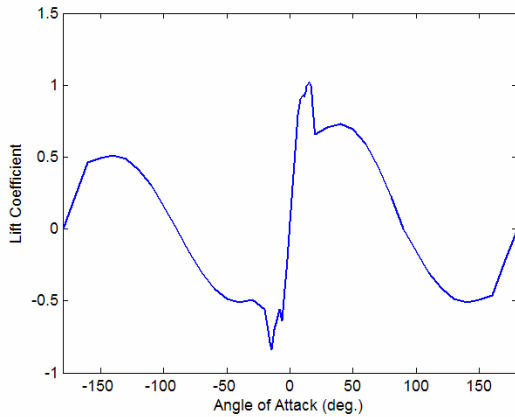


Figure 13. Lift coefficient for S809 airfoil at Reynolds number of 750 million.

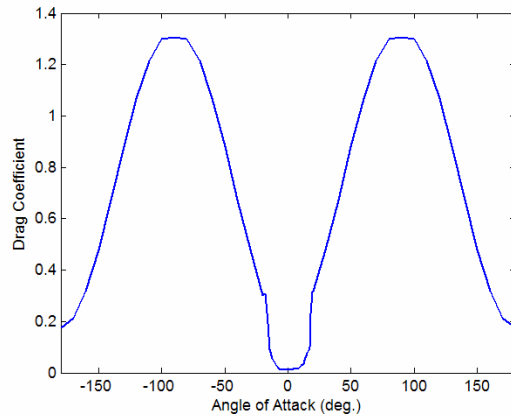


Figure 14. Drag coefficient for S809 airfoil at Reynolds number of 750 million.

to improve the accuracy of airfoil data for modeling real blades in normal wind turbine operating conditions—other than wind-tunnel measurements using the appropriate Reynolds number, surface roughness, and as-built airfoil profile.

Static Airfoil Characteristics

When relying on static airfoil characteristics, the airfoil sections are represented in AeroDyn by tables of lift, drag, and pitching moment (if desired) coefficients as a function of angle of attack and Reynolds number. With these tables, linear interpolation is used to determine the aerodynamic coefficients at a particular angle of attack. Dynamics codes frequently simulate conditions in which the angle of attack of a blade element is well outside the normal operating range of an airfoil. If AeroDyn encounters an angle of attack that is outside the range of the airfoil data table, an error message is generated and program execution stops. For this reason, we recommend that airfoil data tables always cover the entire possible range of angles of attack (-180° to $+180^\circ$).

Often, the aerodynamic coefficients of an airfoil are measured over a limited range of angles of attack and are rarely available over the entire range of $\pm 180^\circ$. In order to generate coefficients over this range, wind tunnel data can be extrapolated by assuming the airfoil behaves like a flat plate at high angles of attack. The advantage of using flat-plate characteristics is that the aerodynamic coefficients depend only on the aspect ratio of the plate. Viterna et al. (1982) developed a method to do this extrapolation and it has been written into an NREL program entitled FoilCheck (Laino and Hansen 2002). Note that this is not a capability of AeroDyn, but the theory is included here for completeness.

Figures 13 and 14 contain aerodynamic coefficient data over an angle of attack range of $\pm 180^\circ$ for an S809 airfoil at a Reynolds number of 750 million. The original data from the wind tunnel test (Ramsay et al. 1995) were measured in a range of angle of attack from -20° to 40° . The remaining values have been calculated using FoilCheck.

From a point just beyond the available data (40° for this case), called the matching point, to 90° the Viterna equations are applied in their original form. The equations are taken from a report by Viterna and Janetzke and are shown below. (Note that there is a typographical error in the equations in the report, but the correct equations are given below.)

$$C_{D_{\max}} = 1.11 + 0.018AR, \quad [98]$$

$$C_D = C_{D_{max}} \sin^2 \alpha + B_2 \cos \alpha, \quad [99]$$

where

$$B_2 = \frac{C_{D_s} - C_{D_{max}} \sin^2 \alpha_s}{\cos \alpha_s}, \quad [100]$$

and subscript s denotes the value at the stall angle or the matching point if data above stall is available. AR is the blade aspect ratio. The lift is given by

$$C_L = \frac{C_{D_{max}}}{2} \sin 2\alpha + A_2 \frac{\cos^2 \alpha}{\sin \alpha}, \quad [101]$$

where

$$A_2 = (C_{D_s} - C_{D_{max}} \sin \alpha_s \cos \alpha_s) \frac{\sin \alpha_s}{\cos^2 \alpha_s}. \quad [102]$$

These equations yield $C_L = 0$ and $C_D = C_{D_{max}}$ at $\alpha = 90^\circ$, and the stall (or matching point) values at α_s . Thus it is important to select α_s carefully. Above 90° and from -180° to the lowest angle of attack with data (-20° in this example), the lift coefficient values are obtained by scaling and reflecting the values from the matching point (40°) to 90° . The scaling and reflections are evident in Figure 13. FoilCheck applies a scaling factor of 0.7 to C_L to account for the asymmetry of the airfoil. That is, all lift values are reduced by 30% from the values between the matching point (40°) and 90° . C_L is forced to zero at $\alpha = \pm 180^\circ$. Drag values are not scaled, just reflected about the zero angle of attack, as seen in Figure 14. Linear interpolation is used to connect the various regions after scaling and reflection.

Pitching moment coefficients can also be extrapolated from tabular data. But the methods used to accomplish this are less rigorous, as described in Hansen and Laino (2002).

Each blade element can have its own airfoil data table, making it straightforward to account for varying airfoil section properties along the blade span. However, at present, all blades must be aerodynamically identical (except the pitch angle).

AeroDyn will accept airfoil data tables that use two inputs: angle of attack and a second parameter that is controlled by the user. This optional parameter could be, for example, Reynolds number or a flap or aileron setting. If the second parameter is Reynolds number, the code will interpolate the airfoil data tables based on the local element Reynolds number. If the second parameter is something other than Reynolds number, the user must provide a separate section of code (such as a controller to determine the aileron setting) that assigns the value of the second parameter. Linear interpolation is also used for intermediate values of the second table lookup parameter.

Dynamic Stall Model

Dynamic stall events are evident from measurement of aerodynamic coefficients on operating wind turbines (as reported in Hansen and Butterfield 1993). Figure 15 illustrates dynamic stall events measured at the 30% span location of the Combined Experiment Rotor. On wind turbine blade airfoil sections, unsteady or oscillatory angle of attack time histories that produce dynamic stall events occur because of the variation in wind velocity over the rotor disk. These variations in velocity are caused by horizontal and vertical wind shears, vertical wind, yaw misalignment, and turbulence in the wind.

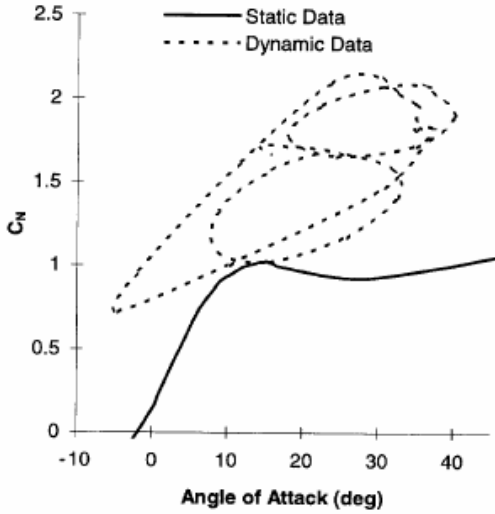


Figure 15. Dynamic stall events measured at the 30% station of the CER (Pierce 1996)

The dynamic stall model of AeroDyn is based on the works of Beddoes and Leishman (1989). Most of the text from this section was taken, essentially verbatim, from two Master of Science theses from the University of Utah by Pierce (1996) and Minnema (1998). These theses provide details on the modification, implementation, and validation of the Beddoes-Leishman dynamic stall model in AeroDyn. In this report we provide a summary, the original theses should be consulted for more details. Also, for the original development of the Beddoes-Leishman model see Leishman and Beddoes (1986, 1989) and Leishman (1989).

The forces used in the Beddoes-Leishman model (normal and chordwise) are slightly different than the forces used in the other models described in previous sections. For clarity, Figure 16 shows the coordinate system and forces used in this model relative to the forces in Figure 3.

The Beddoes-Leishman model is a semi-empirical model that is based on airfoil indicial response. Indicial response produces the normal force coefficient (C_N), and the moment force coefficient (C_M) as a function of time for a step change in angle of attack. The indicial response is derived from the solution of the linearized differential equations for an unsteady, compressible, inviscid fluid (Bisplinghoff et al. 1955). The increment in C_N due to a step change in angle of attack ($\Delta\alpha$) is broken into two components, a non-circulatory component (C_N^I), and a circulatory component (C_N^C), given as

$$\begin{aligned} \Delta C_N^C &= C_{N\alpha} \phi_\alpha^C \Delta\alpha \\ \Delta C_N^I &= \frac{4}{M} \phi_\alpha^I \Delta\alpha \end{aligned} \quad [103]$$

where $C_{N\alpha}$ is the normal force coefficient curve slope, M is the Mach number, ϕ_α^C is the

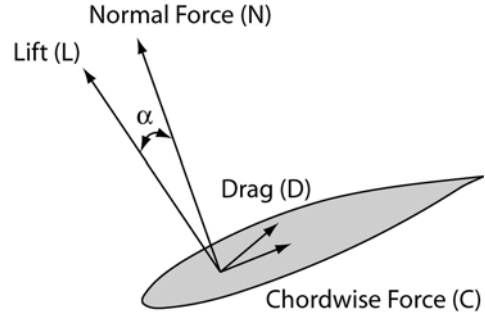


Figure 16. Coordinate system and forces used in dynamic stall modeling

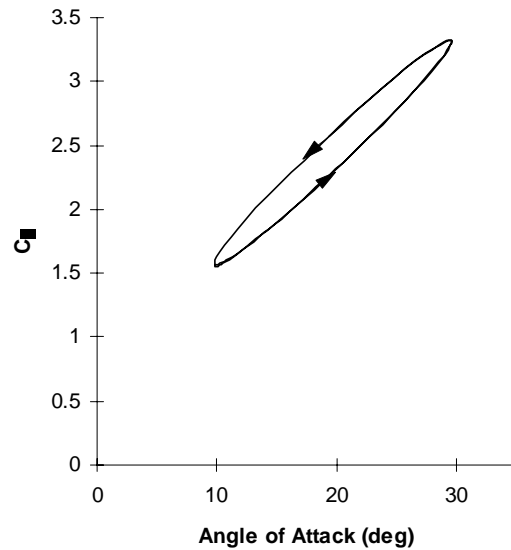


Figure 17. Typical attached flow unsteady response of the normal force coefficient

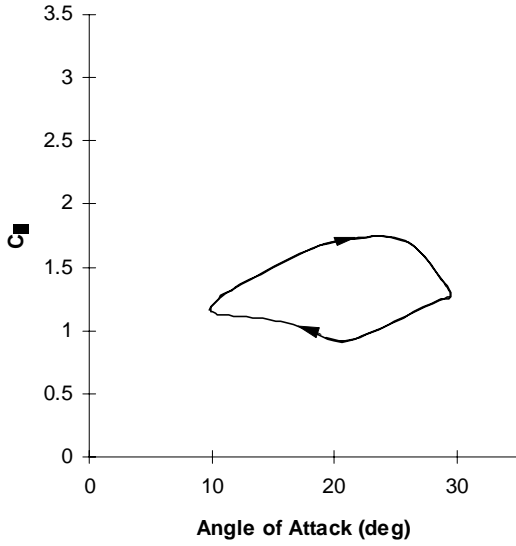


Figure 19. Typical normal coefficient response of an airfoil with attached flow modified by separation point

circulatory indicial function, and ϕ_α is the non-circulatory indicial function. These indicial functions are nearly pure exponential functions and are represented by exponential functions in the model. In the Beddoes-Leishman model, the chordwise force coefficient (C_C) response is based on the circulatory component of C_N . The airfoil attached flow response due to a general angle of attack history is calculated from the superposition of individual indicial responses for each step. A typical C_N hysteresis for an unspecified airfoil with attached flow is shown in Figure 17.

It is important to note that AeroDyn treats all changes in angle of attack equally. This is true whether the changes are due to blade flap or lag motion, pitch motion, or changes in local relative wind velocities.

The calculated attached flow response is then modified based on the position of the effective flow separation point on the low-pressure side of the airfoil. Flow separation from the airfoil results in a loss of circulation about the airfoil, reducing aerodynamic coefficients from the attached flow values. The separation point is given by $f = x/c$, where x is the point of flow separation measured from the leading edge, and c is the airfoil chord length. An approximation to Kirchhoff theory (Thwaites 1960) used by Beddoes relates C_N and C_C to the separation point given as:

$$C_N = C_{N\alpha} (\alpha - \alpha_0) \left(\frac{1 + \sqrt{f}}{2} \right)^2 \quad [104]$$

$$C_C = C_{N\alpha} (\alpha - \alpha_0) \tan(\alpha) \sqrt{f}$$

where α is the angle of attack, and α_0 is the zero-lift angle of attack.

The static effective separation point is calculated from static C_N data by solving Equation 104. The effective separation point versus angle of attack is then curve fit using an exponential function. The parameter f , calculated from Equation 104 using static data, is referred to as the *effective separation point*, since it represents the amount of separation according to

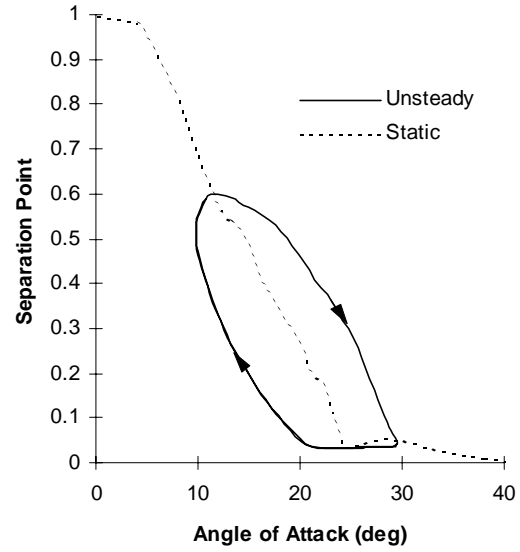


Figure 18. Unsteady separation point curve

Kirchhoff theory, which is an inviscid solution, but it might not necessarily represent the actual point of flow reversal on the airfoil. It does, however, provide a method of representing the effect and dynamics of separation. In the Beddoes model, an empirically derived first order lag is applied to the movement of the effective separation point to account for the time lag in movement of the separation point during unsteady conditions. Figure 18 shows the calculated C_N of an unspecified airfoil including the effects of unsteady separation. The unsteady effective separation point curve is shown in Figure 19.

The final main component of the model represents the vortex buildup and shedding that occurs during dynamic stall. The vortex lift contribution is empirically modeled as an excess circulation in the vicinity of the airfoil. The magnitude of the increase in lift is based on the difference between the attached flow C_N and the

C_N value obtained from the Kirchhoff equation. Empirically derived time constants are used to govern the growth, decay, and motion of the vortex. As the airfoil pitches upward, the vortex strength is allowed to build. When the first-order-lagged, attached-flow C_N (denoted as C'_N) exceeds the C_N value at stall (C_{Nl}), the vortex is allowed to begin convecting across the airfoil. A nondimensional time constant (τ_v) tracks the position of the vortex across the airfoil. As the vortex reaches the trailing edge, the strength is allowed to decay exponentially. The calculated C_N of an unspecified airfoil, including all model components, is shown in Figure 20.

The lift coefficient (C_L) and drag coefficient (C_D) are then calculated from resolving C_N and C_C into components normal and parallel to the velocity direction, and adding the minimum drag (C_{D0}) (see Figure 16).

$$\begin{aligned} C_L &= C_N \cos(\alpha) + C_C \sin(\alpha) \\ C_D &= C_N \sin(\alpha) - C_C \cos(\alpha) + C_{D0} \end{aligned} \quad [105]$$

Model Modifications

Some modifications to the model were necessary to make it applicable to the environment and airfoils of wind turbines. Beddoes considers angles of attack from approximately -10° to 30° ; however wind turbine airfoils often operate outside of this range. Because of this, the model must be capable of producing aerodynamic force coefficients over the entire range of possible angles of attack, which required several modifications to the original model.

To allow the model to reproduce aerodynamic coefficients at high angles of attack, the angle of attack was modified as follows:

$$\begin{aligned} \text{for } |\alpha| \leq 90^\circ \quad \alpha_m &= \alpha \\ \alpha > 90^\circ \quad \alpha_m &= 180^\circ - \alpha \\ \alpha < -90^\circ \quad \alpha_m &= -180^\circ - \alpha \end{aligned} \quad [106]$$

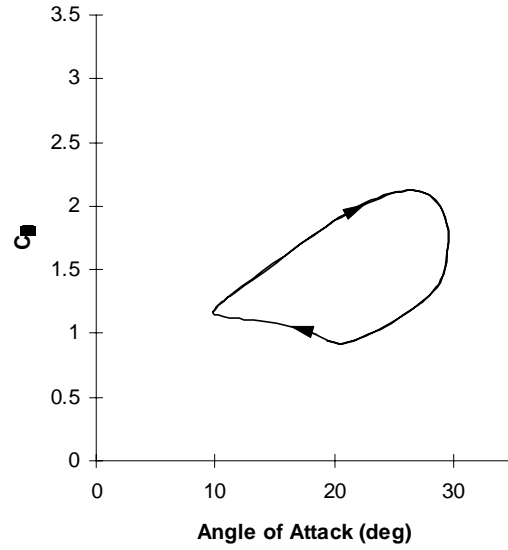


Figure 20. Typical normal coefficient response of an airfoil with attached flow, separation point, and vortex lift contribution

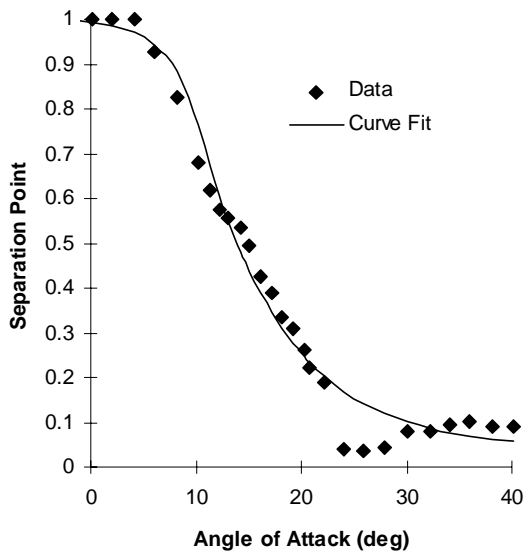


Figure 21. Exponential curve fit to the calculated separation point for a NACA 4415

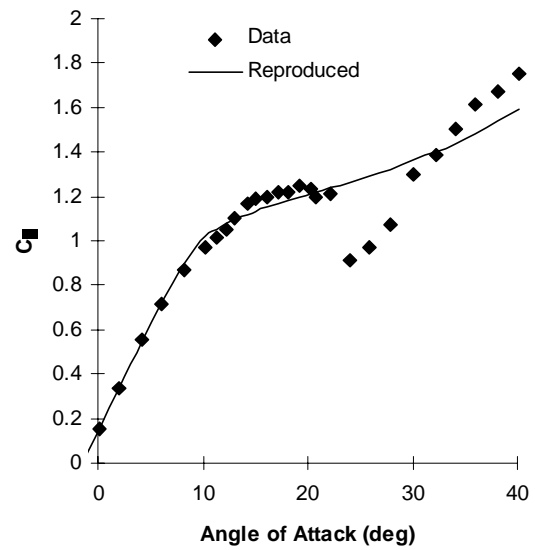


Figure 23. Comparison between data and reproduced curve using exponential curve fit to separation point data (NACA 4415)

where α is the current angle of attack and α_m is the modified angle of attack. The modified angle of attack represents the fact that the normal force coefficient is somewhat symmetric about $+90^\circ$ and -90° . This modified angle of attack is then used to calculate the effective separation point from the Kirchhoff equation; it is also used in the runtime calculation of the attached flow response.

As mentioned previously Beddoes uses an exponential curve fit to the effective airfoil separation point calculated from the static data using Equation 104 and shown in Figure 21. However, this did not work well with some of the airfoils tested. Note that all of the figures in this section (Model Modifications) use measurements of a NACA 4415 airfoil at a Reynolds number of 1 million (Reuss et al. 1995). As can be seen in Figure 22, some important features are lost when regenerating the C_N versus angle of attack curve using the exponential curve fit representation of the effective separation point. For this reason, we used a lookup table in which the calculated effective separation point values are stored with angle of attack values. Linear interpolation is used between points. This method is more applicable to an arbitrary airfoil and accurately reproduces the normal force curve.

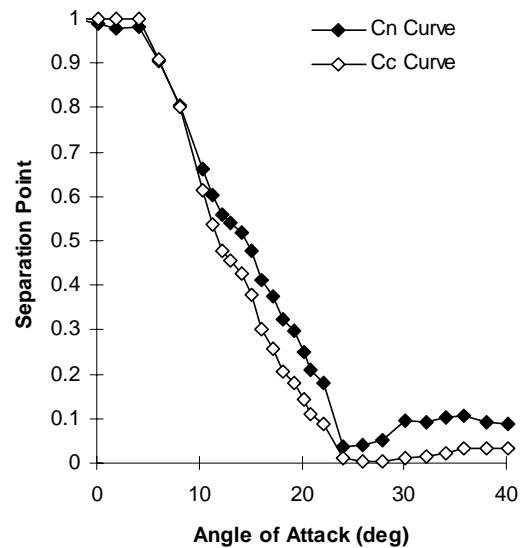


Figure 22. Normal and chordwise coefficient separation point curves for a NACA 4415

Also, upon further investigation into the model, we determined that the calculated C_C value, which was based upon the circulatory component of C_N and the effective separation point calculated using C_N , at times did not reproduce static values. In some angle of attack ranges,

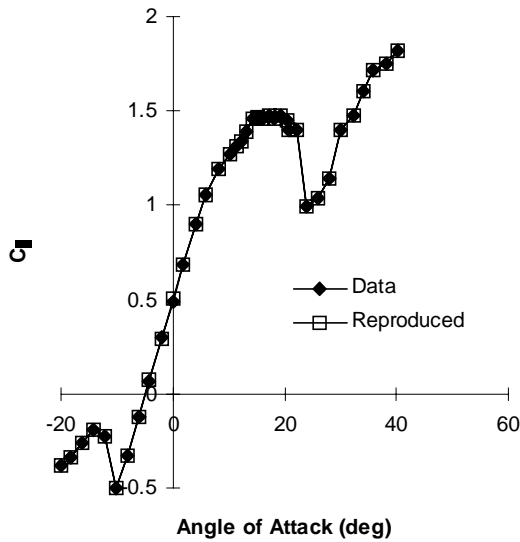


Figure 25. Comparison between measured and reproduced lift coefficient (NACA 4415)

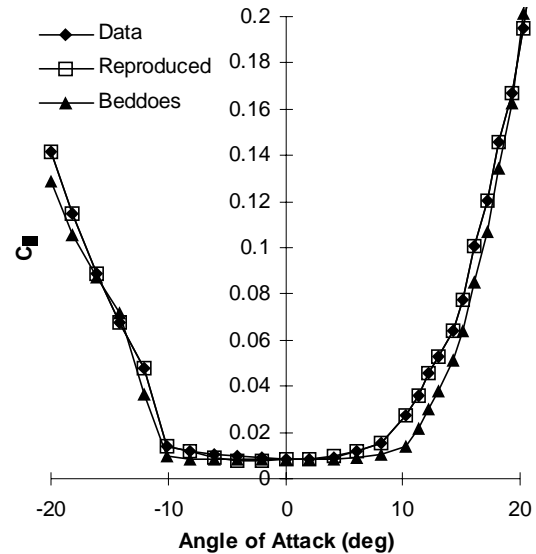


Figure 24. Comparison between measured C_D , C_D reproduced using the current method, and C_D reproduced by method of Beddoes using curve fit C_N separation point (NACA 4415)

the model predicted higher or lower drag because of an error in the prediction of C_C . This resulted in erroneous power output predictions for the rotor. To alleviate this problem two effective separation point tables are calculated, one for C_N and one for C_C . Equation 104 for C_C is used in the calculation of the C_C effective separation point table representing the separation affecting C_C according to Kirchhoff theory. It is also used in the runtime calculation of C_C using the dynamic effective C_C separation point. During unsteady conditions, the same dynamics are applied to each effective separation point. This method allows the model to accurately reproduce static values for very general input values of C_L and C_D .

For most airfoils, the two tables are similar. However, at times there are differences between the two, and even small differences can lead to a significant error in the drag prediction. Figure 23 shows the two effective separation point curves. The model using two effective separation point tables accurately reproduces the static aerodynamic coefficients, as shown in Figures 24 and 25. Figure 25 also reveals that the two-table model is more accurate than the original Beddoes model with only one table.

In Figure 26, dynamic stall hysteresis loops are shown for unusual angle of attack ranges as calculated by the modified method. Because of the lack of test data, the accuracy of the model for high angles of attack is not known. However, the results obtained are at least reasonable.

At angles of attack near $+90^\circ$ and -90° , and occasionally at other locations, the square root of the effective separation point in Equation 104 should be negative to reproduce static aerodynamic coefficient values. This created problems in regenerating the aerodynamic force coefficients since the negative sign is lost when squaring the value to determine the effective separation point. To eliminate this problem, and to ensure proper regeneration of coefficients, the sign of the effective separation point is saved with the value of the parameter. The sign is then used when regenerating aerodynamic coefficients to ensure accurate regeneration. The process of decomposition of the C_N is shown below in Equation 107, and the regeneration given is by Equation 108.

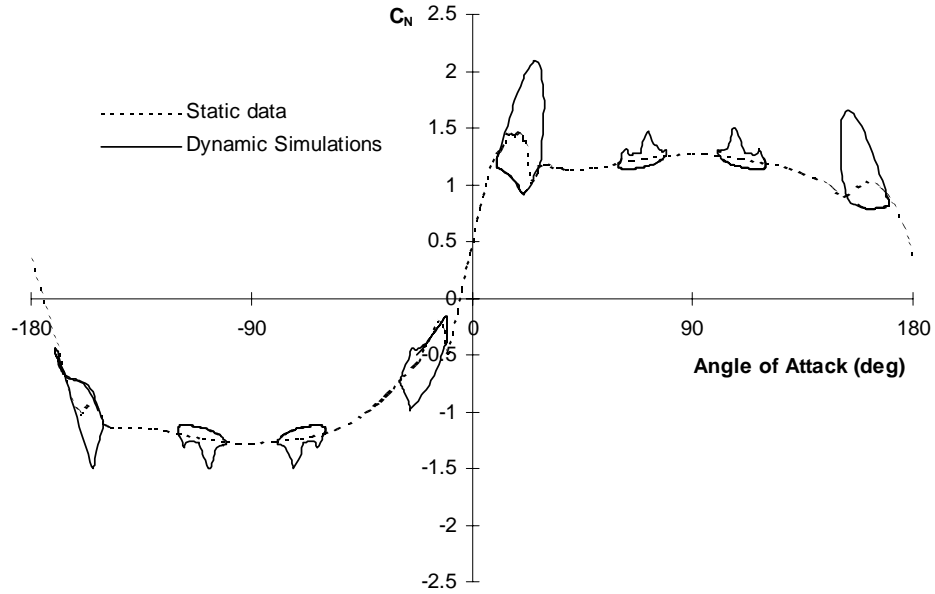


Figure 26. Dynamic normal force coefficient simulations for unusual angles of attack (NACA 4415)

$$t = 4 \sqrt{\frac{C_N}{C_{N\alpha}(\alpha - \alpha_0)}} - 1 \quad [107]$$

$$f = t^2 \text{sign}(t)$$

$$C_N = C_{N\alpha}(\alpha - \alpha_0) \left(\frac{1 + \sqrt{\text{abs}(f) \text{sign}(f)}}{2} \right)^2 \quad [108]$$

Similarly for the C_C , the process of decomposition is shown below in Equation 109, and the regeneration is given by Equation 110.

$$t = \frac{C_C}{C_{N\alpha}(\alpha - \alpha_0)\alpha} \quad [109]$$

$$f_C = t^2 \text{sign}(t)$$

$$C_C = C_{N\alpha}(\alpha - \alpha_0)\alpha \sqrt{\text{abs}(f_C) \text{sign}(f_C)} \quad [110]$$

The calculation of the pitching moment coefficient proceeds along a parallel path. A third “separation point,” f_M , is determined from the static airfoil data. In addition, we found it was necessary to apply a saturation function to limit the impulsive contribution to the pitching moment when the airfoil encounters an abrupt change in angle of attack (e.g. in tower shadow). This is a “patch” that clearly should be replaced by a more accurate calculation of the impulsive terms in the original Beddoes-Leishman formulation. Details can be found in Minnema’s thesis (1998).

Beddoes also includes an empirical separation point shift for the “deep stall regime.” However, whether or not this shifting increases or decreases accuracy depends on the amplitude of

oscillation of the airfoil. For high-amplitude oscillations, including the shift increased the accuracy. However, for low-amplitude oscillations, greater accuracy was obtained without the shift. Also, the shifting was found to cause discontinuities and hence numerical instabilities in force calculations for very small angle of attack oscillation amplitudes. For these reasons the shifting has been removed from the model used in AeroDyn.

For extension to deep stall, Beddoes and Leishman include an additional parameter, Φ , for the correction of the chordwise force during large separations. However, with the current formulation of two effective separation point tables the use of this additional modification seems unnecessary.

Another modification is needed because of parameters that must be triggered and reinitialized at certain locations in the hysteresis. The parameters determine if the vortex strength is building, the time at which the dynamic stall vortex begins to convect over the airfoil, and the position of the vortex. The difficulty arises during general unsteady motion, and at unusual angles of attack when it is unclear whether vortex lift should be added, and when parameters should be reinitialized. As mentioned previously, the vortex is allowed to build in strength as the airfoil pitches toward stall ($+90^\circ$ or -90°). The change in C'_N from one step to the next is used to determine if the airfoil is pitching toward stall. If C'_N is increasing toward stall, a parameter is set to allow the vortex strength to build. C'_N is used since it is less subject to numerical noise than the angle of attack.

The vortex begins to convect across the airfoil when C'_N exceeds C_N . At this time a flag is triggered and the nondimensional parameter τ_v tracks the position of the vortex across the airfoil. Note that τ_v starts at zero when C'_N exceeds C_N , and increases to one when the vortex reaches the trailing edge. After the vortex has passed the trailing edge ($\tau_v > 1$) the vortex strength decays with a time constant equal to half of the value used during accumulation with no further additions to the vortex strength. Then, τ_v is reset to zero if the airfoil begins pitching toward stall after completing a cycle, and the angle of attack changes sign. The parameter τ_v is also reset after a suitable time delay if the airfoil continues pitching toward stall, which allows a secondary vortex to develop and shed using the same dynamics. The frequency of shedding corresponds closely to a Strouhal number of 0.2 (Leishman and Beddoes 1986). If C'_N does not exceed C_N , the vortex strength decays as the airfoil pitches away from stall using a time constant equal to half of the value used during accumulation.

The final modification is a result of the effect of the vortex component on C_C . As mentioned previously, C_C is based on the circulatory component of C_N . However, Beddoes and Leishman do not state whether the vortex component, which is circulatory, should be included in the calculation of C_C . It was apparent from a study of unsteady data that the vortex component contributed to C_C . To model this contribution, we added the vortex component of C_N to C_C in the same manner as the circulatory component of C_N , but also multiplied by $(1 - \tau_v)$. The vortex component was multiplied by $(1 - \tau_v)$, since the effect of the vortex on C_C should depend on the location of the vortex along the chord. Thus, the vortex contributes to C_C in the same manner as the circulatory component of C_N when near the leading edge of the airfoil, but it goes to zero as the vortex reaches the trailing edge. This method produced good agreement with the test data.

Tower Influence

The influence of the wind turbine tower on the blade aerodynamics is also modeled in AeroDyn. The tower influence model is based on the work of Bak, et al. (2001). This model uses a potential flow solution around a cylinder as the base flow field along with a downwind wake

model dependent on tower drag coefficient (based on diameter), C_d , and a tower dam model for upwind influence. The model provides the influence of the tower on the local velocity field at all points around the tower, including increases in wind speed around the sides of the tower and the cross-stream velocity component in the tower near flow field.

Outside of the downwind tower wake, the tower's influence on the nearby dimensionless velocity field is based on these equations:

$$u = 1 - \frac{(x+0.1)^2 - y^2}{((x+0.1)^2 + y^2)^2} + \frac{C_d}{2\pi} \frac{x+0.1}{(x+0.1)^2 + y^2} \quad [111]$$

$$v = 2 \frac{(x+0.1)y}{((x+0.1)^2 + y^2)^2} + \frac{C_d}{2\pi} \frac{y}{(x+0.1)^2 + y^2}, \quad [112]$$

where u and v are the components of the horizontal wind in the x and y direction (in a local, instantaneous, free-stream wind coordinate system), respectively, normalized by the free-stream horizontal wind speed at the point of interest. The parameters x and y are the upwind and cross-wind distances normalized by the tower radius at the height of interest, as seen in Figure 27. Note that the model is dependent upon the drag coefficient of the tower, which can vary over the tower as a function of both the height and the Reynolds number, as specified by the user. This tower influence is used directly as the upwind tower dam effect on the rotor blades.

The local wind velocity outside of the tower wake is thus:

$$U_{local} = uU_{\infty} \quad [113]$$

$$V_{local} = vU_{\infty}. \quad [114]$$

For downwind rotor situations, a tower wake (velocity deficit) model based on the work of Powles (1983) is used. This model is used as an alternative to the wake deficit model provided by Bak, et al. because the Bak model uses a defined width that does not increase with downwind distance, which is not realistic.

The wake factor is determined by these equations:

$$u_{wake} = \frac{C_d}{\sqrt{d}} \cos^2\left(\frac{\pi}{2} \frac{y}{\sqrt{d}}\right) \quad \text{for } |y| \leq \sqrt{d}, \quad [115]$$

where

$$d = \sqrt{x^2 + y^2}, \quad [116]$$

C_d is the drag coefficient of the tower section and d is the dimensionless radial distance of the point of interest from the tower center. The square root of d is also assumed to be the wake width. Figure 27 illustrates these dimensions and the shape of the tower wake. For dimensional consistency in Equation 113, d is normalized by the tower section radius.

If the location is inside the tower wake, as determined by Eqs. 115 & 116, the local velocity in the x direction is

$$U_{local} = (1 - u_{wake})U_{\infty} \quad [117]$$

Whereas the y velocity component remains unchanged from Eqs. 112 & 114 above.

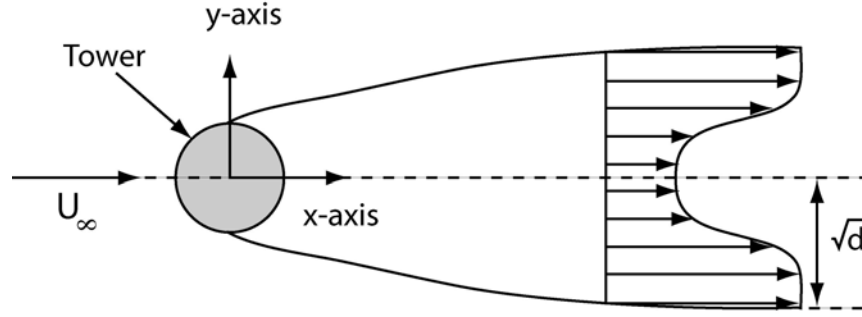


Figure 27. Schematic of the tower shadow model with parameters illustrated for a given point. The tower wake decays in strength and grows in width as the distance from the tower increases.

Note that the wake is assumed to align with the instantaneous horizontal wind vector. This assumption will be improved in a future revision by aligning the wind with a short-term average wind direction. Note also that the wake grows with the square root of the dimensionless distance from the tower centerline. This assumption has not been validated against experimental data, but it is consistent with the wake models of previous versions of AeroDyn (Laino and Hansen 2002). Validation and improvement of the model will occur sometime in the near future.

Wind Input Files

The wind input files of AeroDyn are crucial for determining the wind turbine aerodynamics. AeroDyn obtains wind input data from either simple “hub-height” wind files or from “full-field” wind files that contain turbulent velocity components at points on a grid that covers an area slightly larger than the rotor disc and tower. Both of these files contain information about the velocity field as a function of time and can be created by measurement or simulation.

The simplest wind files, the “hub-height” wind files, contain the hub-height wind speed and direction, vertical and horizontal wind shear coefficients, a vertical component of wind, and a gust velocity. If the file contains only one line of data, those values are used throughout the simulation (steady winds). If the file contains multiple lines of data, linear interpolation in time is performed to obtain the wind speed at a given instant of time at a given location. The ambient wind components at the center of each blade element are determined using the following relations:

$$V_1 = V_{hub} \left[(1 + z/H)^{V_{shr}} + \frac{Hshr(y \cos(\delta - \gamma) + x \sin(\delta - \gamma) + V_{shr_{lin}} z)}{2R} \right] + V_{gust} \quad [118]$$

$$V_x = V_1 \cos(\delta - \gamma) \quad [119]$$

$$V_y = V_1 \sin(\delta - \gamma), \quad [120]$$

where x , y , and z are coordinates (seen in Figure 28) measured from the hub location (x usually points south and z vertical up), γ is the yaw angle of the rotor plane relative to the x -axis, δ is the instantaneous wind direction relative to the x -axis, V_{hub} is the horizontal wind speed at the rotor hub, $Hshr$ and $V_{shr_{lin}}$ are the linear shear coefficients in the horizontal and vertical directions, respectively, V_{shr} is the vertical shear power-law exponent, R is the rotor radius, and V_{gust} is a gust velocity superimposed upon the entire flow field. Each of these wind descriptors can vary in time.

If the user chooses to analyze "full-field" winds, then data files generated by the NREL code TurbSim are typically used. TurbSim generates an array containing all three velocity components at each point on a square grid covering the rotor area as well as points along the turbine tower. To provide a reasonable model of time-varying atmospheric turbulence, winds are typically sampled at 20 Hz. Details on this program can be found in the report by Jonkman and Buhl (2004).

For these "full-field" files, linear interpolation in time and space is used to determine the velocity components at the location of a blade element. It is important to note that interpolation is a form of averaging or smoothing. If the velocities at grid points vary spatially or with time, the velocity at a point midway between two grid points will be the average of the velocities at the two grid points. This means the turbulence intensity at a point in space is a function of the distance between that point and any surrounding grid points. For example, if one does not place a grid point at the center of the rotor (i.e., at the hub), a 6x6 grid measuring 50 m on each side will have a turbulence intensity at the hub that is approximately 1-2 percentage points lower than the values at the central grid points. This effect becomes more pronounced as the distance between grid points increases or as the rotor diameter increases for a fixed number of grid points. For this reason, it may be important to use more grid points for larger rotors.

Possible Improvements

One improvement that will be added to the AeroDyn code in the near future is a stall delay model, which more accurately models three-dimensional rotational augmentation effects, particularly near the blade root. There are several candidates for appropriate modeling of this effect, including the one developed by Du and Selig (1998) and the one created by Eggers et al. (2000). Validation with measured data taken in the NASA Ames wind tunnel experiment (Hand et al. 2001) will be used to determine the best model to implement in AeroDyn. Furthermore, all of the various routines in AeroDyn will be validated and future improvements will be directed on the basis of these results.

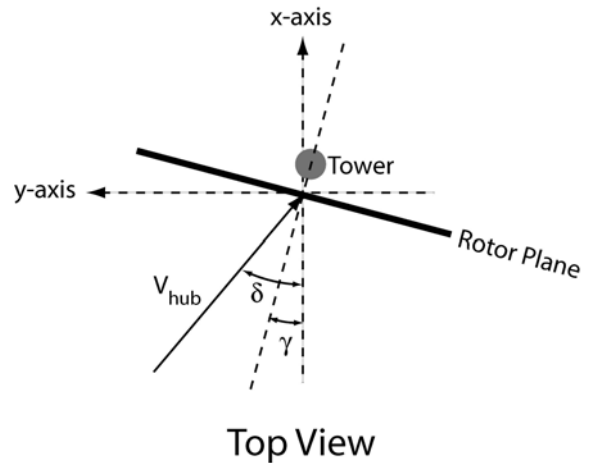


Figure 28. Coordinate system used for wind input files

References

- Bak, C.; Aagaard Madsen, H.; Johansen, J. 2001. "Influence from blade-tower interaction on fatigue loads and dynamics (poster)." *Wind energy for the new millennium. Proceedings. 2001 European wind energy conference and exhibition (EWEC '01)*. Copenhagen (DK), 2-6 Jul 2001. Helm, P.; Zervos, A. (eds.), (WIP Renewable Energies, München 2001) p. 394-397.
- Bisplinghoff, R.L.; Ashley H.; Halfman, R.L. 1955. *Aeroelasticity*, Reading, MA: Addison-Wesley, pp. 332-353.
- Buhl, M.L., Jr. 2004. *A New Empirical Relationship between Thrust Coefficient and Induction Factor for the Turbulent Windmill State*. NREL/TP-500-36834. Golden, CO: National Renewable Energy Laboratory, September.
- Burton, T.; Sharpe, D.; Jenkins, N.; Bossanyi, E. 2001. *Wind Energy Handbook*, New York: Wiley & Sons.
- Coleman, R.P.; Feingold, A.M.; Stempin, C.W. 1945. "Evaluation of the Induced-Velocity Field of an Idealized Helicopter Rotor." *NACA ARR L5E10*.
- Du, Z.; Selig, M.S. 1998. "A 3-D Stall-Delay Model for Horizontal Axis Wind Turbine Performance Prediction." *Proc. 1998 ASME Wind Energy Symposium*. 36th AIAA Aero. Sci. Mtg., AIAA 1998-0021.
- Eggers, A.J. et al. 2000. "Modeling of Yawing and Furling Behavior of Small Wind Turbines," *Proc. 2000 ASME Wind Energy Symposium*. 38th AIAA Aero. Sci. Mtg., AIAA 2000-0020.
- Glauert, H. 1926. "The Analysis of Experimental Results in the Windmill Brake and Vortex Ring States of an Airscrew." *ARCR R&M No. 1026*.
- Glauert, H. 1926. "A General Theory of the Autogyro." *ARCR R&M No. 1111*.
- Glauert, H. 1935. "Airplane Propellers." *Aerodynamic Theory* (W. F. Durand, ed.), Div. L, Chapter XI. Berlin:Springer Verlag.
- Goldstein, S. 1929. "On the Vortex Theory of Screw Propeller." *Proc. Roy. Soc. (A)*, **123**, p. 440.
- Hand, M.M.; Simms, D.A.; Fingersh, L.J.; Jager, D.W.; Cotrell, J.R.; Schreck, S.; Larwood, S.M. 2001. *Unsteady Aerodynamics Experiment Phase VI: Wind Tunnel Test Configurations and Available Data Campaigns*. NREL/TP-500-29955. Golden, CO: National Renewable Energy Laboratory, December.
- Hansen, A.C. 1992. *Yaw Dynamics of Horizontal Axis Wind Turbines*, Final Report. NREL/TP-442-4822. Golden, CO: National Renewable Energy Laboratory.
- Hanson, A.C.; Butterfield, C.P. 1993. "Aerodynamics of Horizontal-Axis Wind Turbines," *Annual Rev. of Fluid Mech.*, **25**, pp. 115-149.
- He, C. 1989. *Development and Application of a Generalized Dynamic Wake Theory for Lifting Rotors*. Atlanta: Georgia Institute of Technology, July.
- Jonkman, B.J.; Buhl, M. L., 2004, *TurbSim User's Guide*. Golden, CO: National Renewable Energy Laboratory.
- Kinner, W. 1937. "Die kreisförmige Tragfläche auf potentialtheoretischer Grundlage." *Ing. Arch*, **8(1)**, pp. 47-80.

- Laino, D.J.; Hansen, A.C. 2002. "User's Guide to the Wind Turbine Aerodynamics Computer Software AeroDyn." Windward Engineering, Salt Lake City, UT, December.
- Laino, D.J.; Hansen, A.C. 2004. "Current Efforts Towards Improved Aerodynamic Modeling Using the AeroDyn Subroutines." *2004 ASME Wind Energy Symposium*, 42nd AIAA Aero. Sci. Mtg., AIAA 2004-0826.
- Leishman, J.G.; Beddoes, T.S. 1986. "A Generalized Model for Airfoil Unsteady Behavior and Dynamic Stall Using the Indicical Method." *Proceedings from the 42nd Annual Forum of the American Helicopter Society*. Washington, DC, pp. 243-266.
- Leishman, J.G.; Beddoes, T.S. 1989. "A Semi-Empirical Model for Dynamic Stall." *Journal of the American Helicopter Society*, **34 (3)**, pp. 3-17.
- Leishman, J.G. 1989. "Modeling Sweep Effects on Dynamic Stall." *Journal of the American Helicopter Society*, **34 (3)**, pp. 18-29.
- Leishman, J.G. 2000. *Principles of Helicopter Aerodynamics*. Cambridge University Press, pp. 78-127.
- Manwell, J.F.; McGowan, J.G.; Rogers, A.L. 2002. *Wind Energy Explained: Theory, Design and Application*. New York: John Wiley & Sons.
- Minnema, J.E. 1998. *Pitching Moment Predictions on Wind Turbine Blades Using the Beddoes-Leishman Model for Unsteady Aerodynamics and Dynamic Stall*. Salt Lake City: Department of Mechanical Engineering, University of Utah.
- Peters, D.A.; He, C.J. 1991. "Correlation of Measured Induced Velocities with a Finite-State Wake Model." *Journal of American Helicopter Society*, July.
- Pierce, K. G. 1996. *Wind Turbine Load Prediction Using the Beddoes-Leishman Model for Unsteady Aerodynamics and Dynamic Stall*. Salt Lake City: Department of Mechanical Engineering, University of Utah.
- Pitt, D.M.; Peters, D.A. 1981. "Theoretical Prediction of Dynamic-Inflow Derivatives." *Vertica*, **5(1)**, March.
- Powles, S.J.R. 1983. "The Effects of Tower Shadow on the Dynamics of Horizontal Axis Wind Turbines." *Wind Engineering*, **7(1)**, pp. 26-42.
- Press, W.H.; Teukolsky, S.A.; Vetterling, W.T.; Flannery B.P. 1992. *Numerical Recipes in FORTRAN (second edition)*. Cambridge University Press.
- Ramsay, R.R.; Hoffman, M.J.; Gregorek, G.M. 1995, *Effects of Grit Roughness and Pitch Oscillations on the S809 Airfoil*. NREL/TP-442-7817. Golden, CO: National Renewable Energy Laboratory, December.
- Reuss, R.L.; Hoffman, M.J.; Gregorek, G.M. 1995, *Effects of Surface Roughness and Vortex Generators on the NACA 4415 Airfoil*. NREL/TP-442-6472. Golden, CO: National Renewable Energy Laboratory, December.
- Simms, D.; Schreck, S.; Hand, M.; Fingersh, L.J. 2001. *NREL Unsteady Aerodynamics Experiment in the NASA-Ames Wind Tunnel: A Comparison of Predictions to Measurements*. NREL/TP-500-29494. Golden, CO: National Renewable Energy Laboratory.
- Snel, H.; Schepers, J.G. (ed.) 1995. *Joint Investigation of Dynamic Inflow Effects and Implementation of an Engineering Method*. ECN-C-94-107, Petten: Energy Research Centre of the Netherlands April.

- Suzuki, A. 2000. *Application of Dynamic Inflow Theory to Wind Turbine Rotors*. Salt Lake City: Department of Mechanical Engineering, University of Utah.
- Tangler, J.L. 2002. *Nebulous Art of Using Wind-Tunnel Airfoil Data for Predicting Rotor Performance*. NREL/ CP-500-31243. Golden, CO: National Renewable Energy Laboratory.
- Thwaites, B. 1960, *Incompressible Aerodynamics*. Oxford University Press, pp. 168-170.
- Viterna, L.A.; Janetzke, D.C. 1982. *Theoretical and Experimental Power from Large Horizontal-Axis Wind Turbines*. NASA TM-82944. Washington, DC: National Aeronautics and Space Administration, September.
- Wilson, R.E.; Lissaman, P.B.S. 1974. *Applied Aerodynamics of Wind-power Machines*. NTIS: PB-238-595. Corvallis: Oregon State University.
- Wilson, R.E.; Patton, E.M. 1978. *Design Analysis of Performance and Aerodynamic Loading of Non-Flexible Horizontal Axis Wind Turbines*. OSU/DOE Report RLO/2227-78-2. Corvallis: Oregon State University, p. 68.
- Xu, G.; Sankar, L.N., 2002. "Application of a Viscous Flow Methodology to the NREL Phase VI Rotor," *Proc. 2002 ASME Wind Energy Symposium*. 40th AIAA Aero. Sci. Mtg., AIAA 2002-0030.